

**Numerical simulation of supersonic flow around civil aircraft
and sonic boom prediction**

A Thesis Submitted

to faculty of School of Aeronautics

Northwestern Polytechnical University

in partial fulfillment of the requirements

for the Degree of Bachelor of Engineering in

Aerospace Engineering

by

DHAKAL AMRIT

2019380021

Advisor: SONG KE

Date: 2023/06/28

ACKNOWLEDGEMENT

I would like to thank Associate Professor SONG KE, my advisor, for his guidance throughout the process and his effort in making me familiar with the concept of grid generation and far field solution calculation and guiding me through the undergraduate dissertation writing.

ABSTRACT

Future supersonic transport will need to address sonic boom reduction, because of the severe rules on noise disturbance. Reducing sonic boom for supersonic aircraft will enable them to fly over land and tap into a large potential market. One of the key technologies for the next generation of eco-friendly supersonic aircraft is to precisely predict and lower sonic boom, which influences the feasibility and profitability of commercial flights. The paper conducts sonic boom prediction of conventional and low sonic boom configuration, based on the next generation of eco-friendly supersonic aircraft, using numerical methods. This study examines the near-field sonic boom prediction of an inviscid supersonic configuration using adaptive-mesh generation refinement procedure. In addition, use propagation tool to find Far field signature. The commercially available CFD software is used for volume mesh generation as well as solver. The obtained CFD solution is compared with experimental results and other numerical simulation obtained from first and second sonic boom prediction workshop.

Keywords: Supersonic civil transport; sonic boom; sonic boom prediction; adaptive mesh refinement; ground signature

摘要

由于噪音干扰的严格规定，未来的超音速运输将需要解决音爆减少问题。减少超音速飞机的音爆将使它们能够飞越陆地，并进入一个巨大的潜在市场。下一代环保超音速飞机的关键技术之一是精确预测和降低音爆，音爆影响着商业飞行的可行性和盈利能力。本文以下一代环保型超音速飞机为基础，采用数值方法对常规和低音爆配置进行了音爆预测。本研究使用自适应网格生成-细化程序来检验无粘性超音速构型的近场音爆预测。此外，使用传播工具来查找远场签名。商用 CFD 软件用于体积网格生成以及求解器。将获得的 CFD 解与第一次和第二次音爆预测研讨会的实验结果和其他数值模拟结果进行了比较。

关键词：超音速民用运输；音爆；音爆预测；自适应网格细化；地面特征

TABLE OF CONTENTS

ACKNOWLEDGEMENT	I
ABSTRACT.....	III
TABLE OF CONTENTS.....	VII
TABLE OF FIGURES	IX
LIST OF TABLES	XII
Chapter 1 Introduction	1
1.1 Research Background	1
1.2 Basic concept of sonic boom	4
1.3 Research progress on supersonic airliner.....	8
1.4 Research progress and status quo of sonic boom prediction methods.....	12
1.5 The purpose and significance of this work	16
1.6 Main content and organization of this paper.....	16
Chapter 2 Approach and Numerical Methods	19
2.1 Nearfield CFD solution.....	20
2.2 Far field solution	23
2.3 Post processing and verification	24
Chapter 3 Nearfield solution.....	25
3.1 69° Delta-Wing-Body (DWB)	25
3.1.1 DWB: Geometry	26

3.1.2 DWB: Meshing	27
3.1.3 DWB: CFD Solution.....	32
3.1.4 DWB: Nearfield solution	35
3.1.5 DWB: Near field comparison with SBPW1	36
3.2 JAXA Wing Body(JWB)	37
3.2.1 JWB: Geometry	37
3.2.2 JWB: Meshing	38
3.2.3 JWB: CFD Solution	43
3.2.4 JWB: Nearfield solution	45
3.2.5 JWB: Near field comparison with SBPW2.....	46
Chapter 4 Far field solution	47
4.1 DWB: Ground propagation.....	47
4.2 DWB: Far field comparison with SBPW1	48
4.3 JWB: Ground Propagation.....	49
4.4 JWB: Far field comparison with SBPW2	51
Chapter 5 Summary and Outlook	52
References.....	54

TABLE OF FIGURES

<i>Figure 1 Sketch of 100-minute economic circle around Beijing (left) and Asia Pacific</i>	
<i>200-minute economic circle(right)^[1]</i>	<i>2</i>
<i>Figure 2 Sonic boom generation, propagation and evolution^[5]</i>	<i>5</i>
<i>Figure 3 Schematic diagram of the formation of primary and secondary sonic boom^[6]...</i>	<i>7</i>
<i>Figure 4 Schematic of sonic boom ground exposures^[5]</i>	<i>7</i>
<i>Figure 5 First generation of supersonic airliners: Concorde (left) and Tu-144(right)</i>	<i>9</i>
<i>Figure 6 Research progress on supersonic passenger aircraft in the United States,</i> <i>Europe and Japan ^[1]</i>	<i>10</i>
<i>Figure 7 Research aircraft for Quiet supersonic technology airliner designed by</i> <i>Lockheed martin(X-59)</i>	<i>11</i>
<i>Figure 8 NASA supersonic goals^[4]</i>	<i>12</i>
<i>Figure 9 Ingredients of sonic boom prediction programs ^[5]</i>	<i>19</i>
<i>Figure 10 Sonic Boom prediction process^[13]</i>	<i>21</i>
<i>Figure 11 69° Delta Wing-Body different views^[18]</i>	<i>26</i>
<i>Figure 12 Wind-tunnel Apparatus Sketch^[17]</i>	<i>27</i>
<i>Figure 13 Initial Mesh Domain around the 69° Delta Wing-Body without support</i> <i>structure</i>	<i>28</i>
<i>Figure 14 Initial Mesh Zoomed view around the 69° Delta Wing-Body without support</i> <i>structure</i>	<i>28</i>

<i>Figure 15 Initial mesh minimum width of 0.02m & data extraction at $H/L=3.6$</i>	<i>29</i>
<i>Figure 16 Initial mesh on DWB surface</i>	<i>29</i>
<i>Figure 17 Final Mesh Domain around the 69° Delta Wing-Body without support structure</i>	<i>30</i>
<i>Figure 18 Final Mesh Zoomed view around the 69° Delta Wing-Body without support structure</i>	<i>31</i>
<i>Figure 19 Final mesh minimum width of 0.001m and data extraction at $H/L=3.6$.....</i>	<i>31</i>
<i>Figure 20 Final mesh on DWB surface</i>	<i>31</i>
<i>Figure 21 69° Delta Wing-Body Mach Line Contours on Pressure coefficient (C_p), Initial mesh, $Mach = 1.7$, $\alpha = 0^\circ$, $\phi=0$, Inviscid solution showing the data extraction line at $H/L= 3.6$.....</i>	<i>33</i>
<i>Figure 22 69° Delta Wing-Body Mach Line Contours on Pressure coefficient(C_p), final mesh, $Mach = 1.7$, $\alpha = 0^\circ$, $\phi=0$, Inviscid solution showing the data extraction line at $H/L= 3.6$.....</i>	<i>34</i>
<i>Figure 23 69° Delta Wing-Body surface Contours on Pressure coefficient (C_p) , Initial & Final mesh, $Mach = 1.7$, $\alpha = 0^\circ$, $\phi=0$, Inviscid solution</i>	<i>34</i>
<i>Figure 24 Final adaptive mesh and initial mesh Pressure distribution (dp/p_{inf}) comparison of 69°Delta Wing,: $M=1.7, \alpha=0^\circ$, $\phi=0$ at $H/L= 3.6$.....</i>	<i>35</i>
<i>Figure 25 All Pressure distribution (dp/p_{inf}) comparison of 69°Delta Wing, CFD vs. Experiment: $M=1.7, \alpha=0^\circ$, $\phi=0$ at $H/L= 3.6$.....</i>	<i>36</i>
<i>Figure 26 Rendering of the supersonic low-boom JAXA Wing Body geometry^[22]</i>	<i>38</i>

<i>Figure 27 Initial Mesh Domain around the JAXA Wing-Body without support structure</i>	39
<i>Figure 28 Initial Mesh Zoomed view around the JAXA Wing-Body</i>	40
<i>Figure 29 Initial mesh on JWB surface</i>	40
<i>Figure 30 Initial mesh minimum mesh width of 0.1m & data extraction at 2.55</i>	40
<i>Figure 31 Final Mesh Domain around the JAXA Wing-Body.....</i>	41
<i>Figure 32 Final Mesh Zoomed view around the JAXA Wing-Body.....</i>	41
<i>Figure 33 Final mesh on JWB surface</i>	42
<i>Figure 34 Final mesh minimum mesh width at data extraction of 0.05 m</i>	42
<i>Figure 35 JAXA Wing-Body Mach Line Contours on Pressure coefficient(C_p), initial mesh, Mach=1.6, $\alpha=0^\circ$, $\phi=0^\circ$, Inviscid solution showing the data extraction line at $H/L= 2.55$</i>	44
<i>Figure 36 JAXA Wing-Body Mach Line Contours on Pressure coefficient(C_p), final mesh, Mach=1.6, $\alpha= 0^\circ$, $\phi=0^\circ$, Inviscid solution showing the data extraction line at $H/L= 2.55$</i>	44
<i>Figure 37 JAXA Wing-Body surface Contours on Pressure coefficient(C_p) , initial mesh& Final mesh, Mach = 1.6, $\alpha = 0^\circ$, $\phi=0^\circ$, Inviscid solution</i>	45
<i>Figure 38 Final adaptive mesh and initial mesh Pressure distribution (dp/p_{inf}) comparison of JAXA Wing,: $M=1.6, \alpha=0^\circ$, $\phi=0^\circ$ at $H/L= 2.55$.....</i>	45
<i>Figure 39 All Pressure distribution (dp/p_{inf}) comparison of JAXA Wing, My CFD vs. SBPW2: $M=1.6, \alpha=0^\circ$, $\phi=0^\circ$ at $H/L= 2.55$</i>	46
<i>Figure 40 Final adaptive mesh and initial mesh Ground signature comparison of 69°Delta Wing,: $M=1.7, \alpha=0^\circ$, $\phi=0^\circ$ at an altitude of 16764m(55000 ft)</i>	47

<i>Figure 41 Final adaptive mesh Ground signature comparison of 69° Delta Wing, My CFD vs. SBPW1 (Aftomis CFD): $M=1.7, \alpha=0^\circ, \phi=0^\circ$ at $H/L=3.6$.....</i>	<i>49</i>
<i>Figure 42 Final adaptive mesh and initial mesh Ground signature comparison of JAXA Wing,: $M=1.6, \alpha=0^\circ, \phi=0^\circ$ at an altitude of 15760 m.....</i>	<i>50</i>
<i>Figure 43 Final adaptive mesh Ground signature comparison of JAXA Wing, My CFD vs. SBPW2: $M=1.6, \alpha=0^\circ, \phi=0^\circ$ at $H/L=2.55$.....</i>	<i>51</i>

LIST OF TABLES

<i>Table 1 Explanation of each parameter in formula (2.1) and formula (2.2).....</i>	<i>20</i>
<i>Table 2 DWB Initial mesh cell count</i>	<i>29</i>
<i>Table 3 DWB final mesh cell count.....</i>	<i>32</i>
<i>Table 4 JWB Initial mesh cell count</i>	<i>39</i>
<i>Table 5 JWB final mesh cell count.....</i>	<i>42</i>

Chapter 1 Introduction

1.1 Research Background

Travel times have accelerated and relationships between nations have gotten stronger as the "global village" has shrunk in the twenty-first century. High-speed subsonic civil aircraft are currently the main means of transportation for crossing international borders. However, the lengthy flight time gravely jeopardizes the comfort and effectiveness of travel, necessitating the urgent need for speedier aircraft. The function of supersonic aircraft in civil aviation is comparable to that of "high-speed railways" in rail systems and "highways" in highway systems. Compared to traditional subsonic aircraft, supersonic aircraft can drastically reduce flying times and improve travel efficiency. The flight duration at a comparable distance for a supersonic aircraft with a cruising Mach number of 2 is roughly 0.45 times that of the fastest subsonic aircraft currently available. Traveling more quickly can improve international contacts and cooperation in the political, economic, cultural, and other spheres. The development of economic globalization and China's national "Belt and Road" building are accelerated by this. Supersonic aircraft are essential for advancing national economic development and improving the quality of life for citizens in places like China and the Asia Pacific area, for instance. They contribute to the formation of the Asia Pacific 200-minute economic circle and the 100-minute economic circle for the capital (Figure 1). As a result, the development of future civilian aircraft has increasingly been influenced by supersonic aircraft^[1].

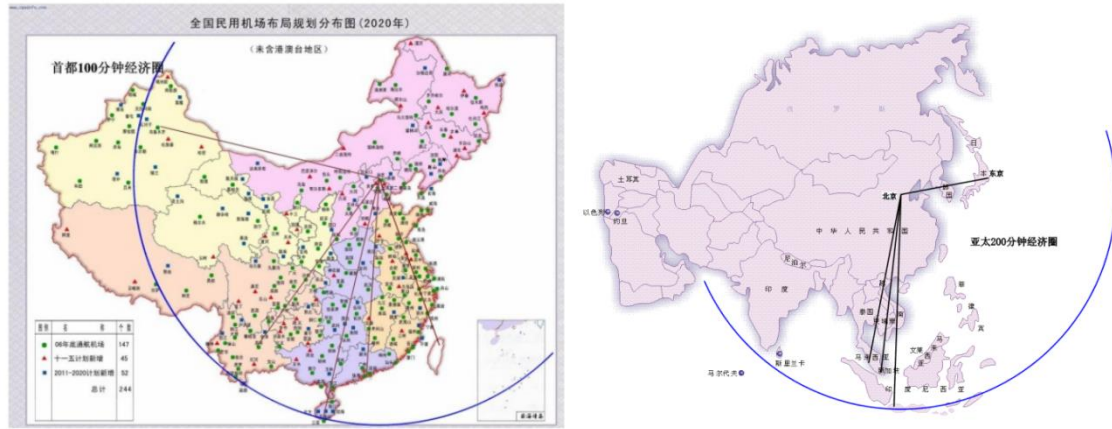


Figure 1 Sketch of 100-minute economic circle around Beijing (left) and Asia Pacific 200-minute economic circle(right)^[1]

Globally, work on developing supersonic aircraft began as early as the 1960s. The United States of America, France, the former Soviet Union, and Britain, in that order, initiated development programs for the first generation of supersonic airliner. The "Tu-144" of the former Soviet Union and the "Concorde" of France and Britain entered commercial service in the 1970s, respectively. However, due to issues like high sonic boom intensity (the ground sonic boom of the Concorde cruise phase can reach 108 PLdB^[2], poor economy, and poor safety after being put into commercial operation, both types of aircraft eventually withdrew from the civil aviation market due to the limitations imposed by the historical background and technological level at the time. At this point, there are still no authoritatively worked supersonic traveler planes globally. This is because there are a lot of major issues with current supersonic aircraft, one of which is the issue of too much sonic boom intensity during the cruise phase. NASA asserts that, in cruise mode, the sonic boom sensation sound pressure level (PLdB) of future supersonic passenger aircraft should not exceed 70 PLdB^[3,4], whereas the current international advanced level can only be reduced

to 80-85 PLdB. As a result, the primary issue that needs to be resolved is the excessive sonic boom intensity that supersonic aircraft cause during flight.

High-precision sonic boom prediction methods and effective low sonic boom optimization techniques have emerged as essential technologies for reducing the level of sonic boom and resolving the issue of supersonic passenger planes experiencing excessive sonic boom intensity during the cruise phase. The obvious sonic boom that occurs during supersonic flight was mentioned in the introduction of the "Centennial Series of Fighters" in the 1950s. After that, numerous nations began to pay a lot of attention and do a lot of research to learn more about ground sonic booms and reduce their intensity^[4]. The foundation for suppressing sonic booms and designing low sonic booms is an understanding of the sonic boom phenomenon and the application of high-precision prediction methods for evaluation. The optimization design process for low sonic booms lacks credibility and engineering value without reliable sonic boom analysis as a prerequisite. High-precision sonic boom prediction techniques have benefited from the development of computational fluid dynamics (CFD) technology in recent years. However, high reliability CFD analysis requires a significant amount of computation. The optimization process will be difficult if the low sonic boom optimization design makes frequent use of high-precision sonic boom analysis. In order to address the issue of excessive sonic boom intensity in the new generation of supersonic aircraft and encourage the early realization of commercial supersonic aircraft operation, the development of effective low-sonic boom optimization design methods and high-precision sonic boom prediction methods has significant theoretical and engineering application value.

1.2 Basic concept of sonic boom

Sonic boom is a special acoustic phenomenon produced during the supersonic flight of aircraft, which is an effect caused by the compression of shock waves on the air. After the shock wave is compressed and expanded, the atmospheric pressure at the shock wave increases and then decreases, and then returns to the atmospheric pressure. In this process, with the propagation of the shock wave, the pressure shape will gradually form an N-shape, called N-shape wave. The sonic boom prediction method introduced later is the prediction of N-shaped waves. The sonic boom can be divided into three distinct regions: near-field region, mid-field region and far-field region. As depicted in (Figures 2), the overpressure value in the time series forms an N-type wave in the region where the front and rear shock waves pass. Overpressure value and rise time and duration are the parameters that describe N-type waves. The rise time is the amount of time the pressure step of the shock wave must travel before the sonic boom; the length alludes to the amount of time that the sound blast unsettling influence encounters from the very beginning as far as is possible. The overpressure value is the difference between the maximum pressure disturbance caused by a sonic boom and the pressure in the environment. The rise time, which has a significant impact on the analysis of the sonic boom spectrum and the subjective noise level calculation, is one of these three parameters that plays a very important role in determining the low sonic boom design of supersonic aircraft and measuring the intensity of ground sonic booms. The magnitude of the overpressure value of the ground sonic boom is 50-150 Pa (1.0-3.0 psf) when a typical supersonic aircraft is flying at cruising altitude. Because of the presence of two shock waves when a sonic boom, individuals for the most part hear two booms. However, at $t = 0.1s$, the human ear is unable to differentiate between the

pressure changes brought on by the shock waves from the front and the back, and only one boom sound is heard^[4].

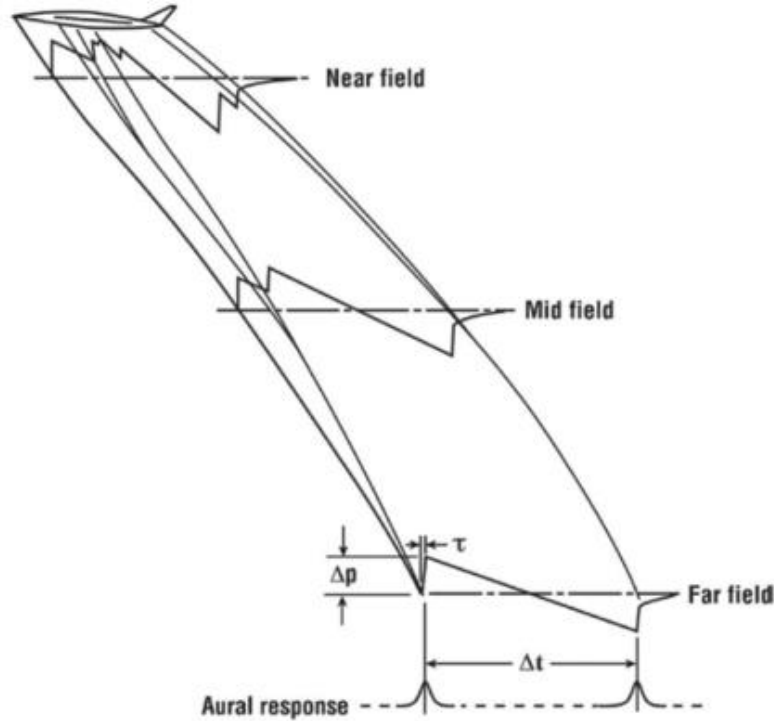


Figure 2 Sonic boom generation, propagation and evolution^[5]

The primary impact area (also known as the major impact area) and the secondary impact area are the two main regions of the sonic boom that are created when a supersonic aircraft is cruising. Figure 3 depicts the scenario after a series of rays propagating in the atmosphere are projected onto a plane perpendicular to the flight direction. It shows the formation of the primary and secondary impact domains of a sonic boom. The major area of influence, also known as the "sonic boom blanket," is the area of the sonic boom that spreads from the body to the ground along the solid line in the illustration. A multitude of variables, including flying altitude, cruising Mach number, and atmospheric wind profile, have an impact on the primary influence domain's size. The propagating rays of the sonic boom

above the body and the propagating rays of the primary sonic boom reflected on the ground will bend toward the ground in the atmosphere due to the layering effect of the atmosphere, as indicated by the dotted line in the picture. The secondary influence domain is the term used to describe the influence region that forms when a portion of the sonic boom that is traveling along the ray indicated by the dotted line in the illustration reaches the ground. Normal conditions lead to a secondary sonic boom with a low frequency (0.1–1.0 Hz), which is undetectable to the human ear. However, in extreme cases, the secondary sonic boom may harm both buildings and people due to its ability to reverberate with animal organs.

The shock wave will focus under specific conditions when the aircraft accelerates at supersonic speed, and super-boom events will be seen at some observation places on the ground in addition to the primary and secondary impact domains of the sonic boom in the supersonic cruising stage. It has a waveform that resembles the letter "U," or a U-shaped wave. U-type waves can have an overpressure value that is 2 to 5 times more than that of N-type waves, and they are often stronger than N-type waves. The effect of a sonic boom on the ground when an aircraft transitions from subsonic to supersonic speed and back again is seen in (Figure 4).

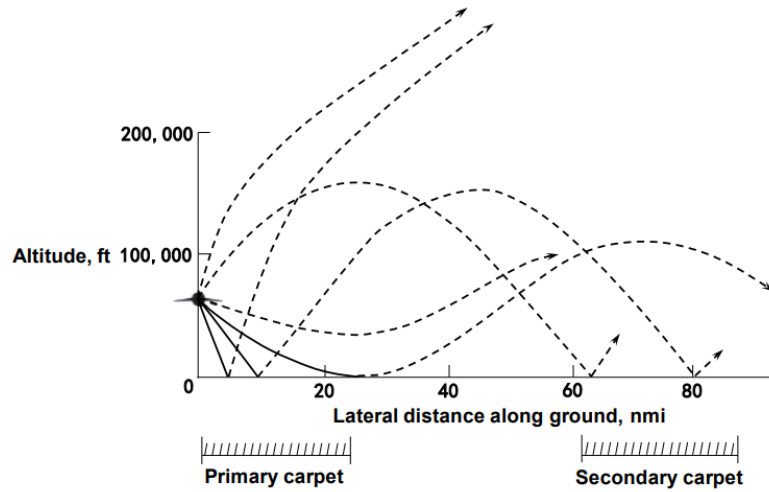


Figure 3 Schematic diagram of the formation of primary and secondary sonic boom^[6]

The primary sonic boom and its influence domain are the main focus of the current process of developing supersonic aircraft due to the high intensity and broad range of influence of the primary sonic boom during the cruise phase of supersonic aircraft. Therefore, the major sonic boom is the subject of most of the study in this dissertation.

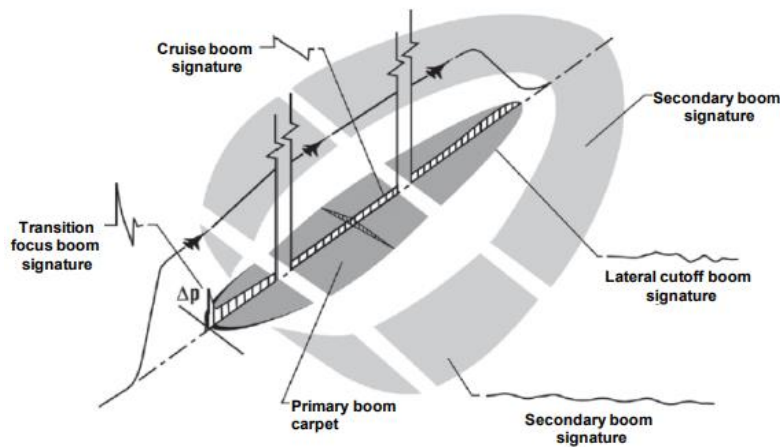


Figure 4 Schematic of sonic boom ground exposures^[5]

1.3 Research progress on supersonic airliner

On October 14, 1947, the X-1 test aircraft, piloted by American pilot Yegor, broke through the sound barrier for the first time at an altitude of 13000 m. Since then, human exploration of supersonic flight has never stopped. From supersonic military aircraft to supersonic civil aircraft is the inevitable result of human exploration of supersonic travel. Compared with subsonic and high-subsonic airliners, supersonic airliners can significantly reduce flight time. The United States, the Soviet Union, the United Kingdom and France have been studying supersonic airliners since the 1960s. However, due to serious environmental problems such as aerodynamic noise and sonic boom, the first generation of supersonic airliners (such as Concorde) died early. Now, due to the optimistic prospect of the future civil market, countries such as Europe, America and Japan are conducting in-depth research on the second-generation supersonic passenger aircraft.

The research and development of supersonic passenger aircraft in foreign countries is mainly divided into three categories: Europe, the Soviet Union and the United States, and the development stage is divided into the first generation of supersonic passenger aircraft and the second generation of supersonic passenger aircraft. With the service of supersonic fighter aircraft, in the mid-1950s, in order to pursue the travel speed on both sides of the Atlantic, Britain and France began to develop supersonic passenger aircraft, and successively put forward the design scheme of the 223 plan and the design scheme of the super sail. In order to compete with the Boeing 707 and Douglas DC-8 at that time, in the 1960s, Britain and France began to cooperate in the development of the "Concorde" airliner(shown in Figure 5),, which first flew in March 1969. It was put into service in 1976, but was retired in 2003 due to environmental and economic problems. During the same

period of the development of "Concorde", the Soviet Union also began to develop supersonic passenger aircraft. In December 1968, Tu-144(shown in Figure 5), made its first flight and broke through the sound barrier for the first time in June 1969. As a superpower, the United States is not to be outdone in the development of supersonic airliners. Boeing began to research supersonic airliners in 1952. In the 1960s, the United States began to implement the SCAT plan and the NST plan, and carried out a deeper research on supersonic airliners^[5].



Figure 5 First generation of supersonic airliners: Concorde (left) and Tu-144(right)

However, the economic and environmental problems of this generation of supersonic passenger aircraft, especially the sonic boom problem, led to its failure. In 70s, when the awareness of environmental protection was growing, countries gave up the research on the first generation of supersonic airliners. However, the desire for supersonic travel still exists. In the late 70s, research on the second-generation supersonic passenger aircraft began gradually.

The approaches for predicting sonic booms have advanced in research and are currently in the status quo. A new generation of supersonic passenger aircraft is the subject of intense global research thanks to the development of aviation technology and studies on supersonic

flight-related topics. Figure 6 illustrates the state of current international research on supersonic passenger aircraft. The HSR (high speed research) plan, QSP (quiet supersonic platform), NEXST plan, "N+3" plan, and other research programs with a time frame of more than 30 years have been developed by the United States, Japan, Europe, and other nations. In the past 15 years, NASA has spent at least US\$1.8 billion on research on a new generation of supersonic passenger aircraft technology, to use the United States as an example. Additionally, the likes of Boeing and Lockheed Martin, which represent the aviation industry, have made significant investments in the study of supersonic passenger planes. It is noteworthy that the US BOOM Company finished the BOOM Airliner's design in 2016 and has just finished producing and testing the XB-1 low-sonic boom verification equipment in a wind tunnel. In addition, Lockheed Martin of the United States, in cooperation with NASA, has realized the test flight of the X-59 (Figure 7) supersonic passenger aircraft verification aircraft in 2021, and formulated the ground sonic boom level standard for supersonic passenger aircraft cruise^[1].

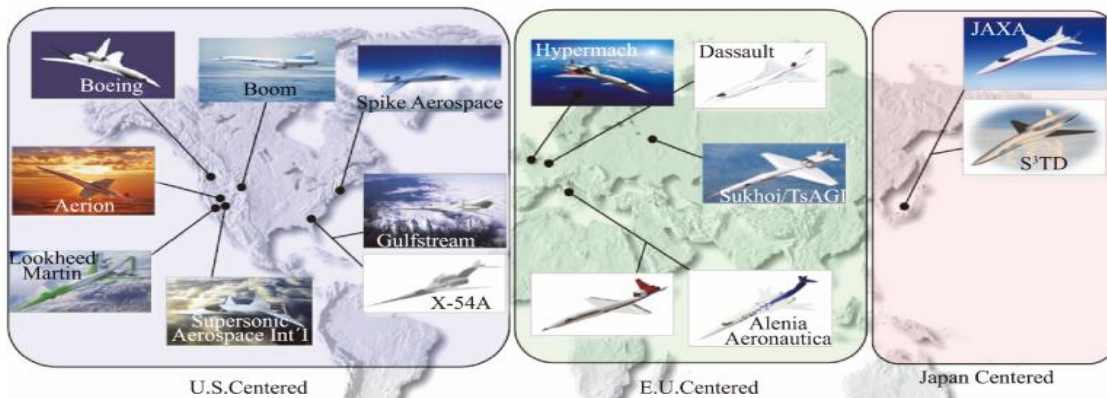


Figure 6 Research progress on supersonic passenger aircraft in the United States, Europe and Japan ^[1]

The IFAR international cooperation project in the aviation field was established in 2010, and the United States, Russia, Japan, Germany, France and other countries all participated in it. At present, a lot of research on supersonic passenger aircraft is also carried out. According to the "N+3" plan formulated by NASA, in the next 10 years, the United States will develop a small supersonic business jet that can be put into commercial operation, and in the next 20 years or so, it will develop a large supersonic jet with 100-300 seats. In the "N+3" plan, there are clear requirements for the technical indicators of supersonic passenger aircraft at each stage, as shown in Figure 8. The table in the picture shows that the new generation of supersonic passenger aircraft has made resolving the issue of excessive sonic boom intensity a top priority. This issue was unrelated to the first generation of supersonic passenger aircraft. The stipulation that the sonic boom level should not exceed 70 PLdB in the NASA "N+3" plan remains of reference value even if the International Civil Aviation Organization has not yet published a standard for the sonic boom intensity of supersonic passenger aircraft. However, the sonic boom intensity of cutting-edge supersonic aircraft studied internationally can only reach 80–85 PLdB. As a result, lowering the intensity of sonic boom produced by supersonic passenger aircraft is an extremely tough problem that still needs to be solved [3].



Figure 7 Research aircraft for Quiet supersonic technology airliner designed by Lockheed martin(X-59)

	N+1 Supersonic Business Class Aircraft (2015)	N+2 Small Supersonic Airliner (2020)	N+3 Efficient Multi-Mach Aircraft (Beyond 2030)
Environmental Goals			
Sonic Boom	65-70 PLdB	65-70 PldB	65-70 PLdB low boom flight 75-80 PLdB unrestricted flight
Airport Noise (cum below stage 3)	10 EPNdB	10-20 EPNdB	20-30 EPNdB
Cruise Emissions (Cruise NOx g/kg of fuel)	Equivalent to current Subsonic	< 10	< 5 & particulate and water vapor mitigation
Performance Goals			
Cruise Speed	Mach 1.6-1.8	Mach 1.6 -1.8	Mach 1.3 - 2.0 low boom flight Mach 1.3- 2.0 unrestricted flight
Range (n.mi.)	4000	4000	4000 - 5500
Payload (passengers)	6-20	35-70	100 - 200
Fuel Efficiency (passenger-miles per lb of fuel)	1.0	3.0	3.5 – 4.5

Figure 8 NASA supersonic goals^[4]

1.4 Research progress and status quo of sonic boom prediction methods

Sonic boom prediction includes the process of near-field and propagation from near-field to far-field, the description of ray path in non-uniform atmosphere with wind, the calculation of ray tube area and its important meaning, the calculation of decay time variable and the correction of nonlinear term. Whitham and Hayes ^[7,8] have established a complete set of methods to predict the sonic boom, but they have not put forward substantive suggestions for the design of supersonic aircraft, and because the description of nonlinear terms is not accurate enough, the error is relatively large.

Linearization theory is relatively complex in terms of calculation, and it invests too much in the early prediction. In order to alleviate this contradiction, H.W. Carlson^[9] established a semi-quantitative prediction method, SSBP (Simplified Sonic-Boom Prediction), in 1978.

The parameters involved in the method are obtained by fitting a large number of experimental data, which can be used to calculate the sonic boom generated by the aircraft during supersonic flight in a steady atmosphere. However, for the results calculated by this method, the error is also relatively large, and in the prediction, due to the inaccurate description of the F-function, no design suggestions for the design of supersonic aircraft have been put forward. In order to solve the problem that linearization theory cannot provide design suggestions for supersonic aircraft design, Seepass-George-Darden (SGD) method^[10] was proposed and research on boom prediction methods. In fact, with the advent of supersonic fighters, the research on sonic booms began as early as the 1950s. Whitham and Hayes were the first to study it. They established and improved the linearization theory of supersonic sonic boom, and described the sonic boom phenomenon with improved by Seepass-George-Darden and later Darden in 1972^[7,8]. This method is based on the linearization theory proposed by Whitham and Hayes, and realizes the optimization design of aircraft shape by optimizing the F-function closely related to sonic boom. Compared with the linearization theory, the SGD method provides substantive guidance for the optimization design of supersonic aircraft sonic boom. However, because SGD is based on the linearization theory, it has the inherent defects of the linearization theory.

Whitham^{[7][25]} founded the linear acoustic explosion prediction theory. Through the assumption of weak shock waves and modifications to the linear supersonic flow theory, the F-function is used to represent the acoustic disturbance source and describe the formation process of far-field N-type waves. Among them, the calculation of the F function involves the equivalent cross-sectional area of the body of revolution, which is obtained from a series of planes cut by the Mach cone in front of the observation point. Afterwards,

Keller^[26] introduced geometric acoustic methods into the propagation of weak shock waves, further improving the calculation accuracy of far-field acoustic explosion waveforms. In the far-field acoustic explosion calculation of the lift body model, Walkden^[27] added the contribution of lift to the acoustic explosion to the F-function calculation and provided the F-function calculation results for a simple wing body combination model with lift. By the early 1960s, the basic theory of linear acoustic explosion prediction was initially established, which could calculate the propagation results of acoustic explosions in a stratified atmosphere under any maneuvering action of an aircraft. However, due to the inherent limitations of linear acoustic explosion prediction theory, the shock wave positions in the calculated far-field acoustic explosion signals are strongly discontinuous. In order to make the waveform more in line with the real situation and to analyze the noise level of far-field acoustic explosions, there are generally two methods for handling discontinuities. One is the acoustic explosion frequency domain solution method developed by Pestorius^[28] and Anderson^[29], and the other is the shock wave correction method^{[30][31]}. After the basic establishment of sonic boom prediction theory, multiple sonic boom prediction programs have emerged internationally. In 1963, Friedman et al.^[32] developed a sound boom prediction program and applied it to the sound boom evaluation of NASA's then SST program Boeing 2707, marking the beginning of the era of sound boom prediction programs. Although the program included very detailed modifications, it contradicted the expression of ray tube area in geometric acoustics. In 1969, Hayes et al.^[33] developed the ARAP program to effectively solve these problems, taking into account the characteristics of the F function as a source of sound explosions, and providing a detailed calculation form for ray paths in geometric acoustics. In 1972, Thomas^[34] developed a

waveform parameter method for calculating far-field waveform signals using algorithms different from Hayes et al., and the calculation results were consistent with those of ARAP. In order to simplify the process of acoustic explosion calculation, in 1978, Carlson^[8] developed a simplified acoustic explosion prediction method through theoretical analysis and a large amount of flight test statistical data, replacing the factors that affect the intensity of acoustic explosions with several key factors. Although this method has fast calculation speed, its calculation accuracy depends on the flight test database, and there is a significant error in acoustic explosion evaluation when targeting new layout forms of aircraft. In 1980, Taylor^[35] developed the TRAP program based on ARAP, which smoothed the waveform of far-field N-type waves at the shock by adding shock type corrections, make the waveform more realistic. In 1995, R.O. Cleveland^[11] put forward a sonic boom prediction method based on Burgers equation on the basis of predecessors, and made a more reasonable explanation for the nonlinear term. In 1998, Plotkin^[36] developed the PCBoom3 program based on the Thomas waveform parameter method, which also used the same method to handle waveform discontinuities. Later, Sriram K. Rallabhandi^[12] proposed an advanced prediction method based on Burgers augmented equation, forming the sBOOM algorithm.

In recent years, the high-precision sonic boom prediction theory based on CFD has also gradually developed. This method considers that the use of F-function as the acoustic source characteristics of aircraft has certain limitations, and proposes near-field pressure as the acoustic source characteristics to describe the aircraft sonic boom, thus improving the accuracy of sonic boom prediction.

1.5 The purpose and significance of this work

Due to the failure of the first generation supersonic airliner, the second-generation supersonic airliner focused on the environmental problems of sonic boom. The sonic boom prediction is of great significance to the aerodynamic optimization of supersonic passenger aircraft. We can use the sonic boom prediction method to predict the sonic boom generated during the supersonic flight of the aircraft, and use the sonic boom minimization theory or other design theories to optimize the aerodynamic performance of the supersonic aircraft to meet the sonic boom requirements. In this process, an effective and accurate sonic boom prediction plays a key role, which also leads to my work on accurate sonic boom prediction methods.

1.6 Main content and organization of this paper

This paper mainly focuses on key technologies that urgently need breakthroughs in sonic boom prediction and suppression during the development of supersonic passenger aircraft.

Research in the following three areas:

(1) In view of the demand for rapid assessment of sonic boom in the conceptual design and preliminary design stages of supersonic passenger aircraft, research the rapid prediction method of sonic boom. This paper mainly focuses on the simplified sonic boom prediction using currently available commercial CFD technology (named CFD software) to calculate near-field sonic boom signal.

(2) For the detailed design stage of supersonic passenger aircraft, research the high-precision prediction method of sonic boom. This paper mainly focuses on the calculation of near-field sonic boom based on CFD and the prediction method of far-field sonic boom

based on nonlinear Burgers equation. The sonic boom prediction program (named bBoom) has been used for calculation of the far-field sonic boom waveform.

(3) Aiming at the design of high-efficiency global low-sonic boom of supersonic airliner. This paper mainly focuses on the calculation and verification of near field and far field sonic boom of each cases from first and Second SBPW.

The structure of this article is as follows:

The introduction is found in the first chapter. This paper primarily introduces the research background of the low sonic boom and the sonic boom prediction method, describes the research status of supersonic passenger aircraft, , and provides the work content.

The Numerical sonic boom prediction method is the main topic of the second chapter. Introduce the CFD approach, the equations involved, and the soft wares used for near field signature briefly. Then, post processing for the far-field sonic boom. Finally, use sonic boom propagation tool to get the far field propagation or ground signature.

The third chapter primarily investigates the CFD-based near-field sonic boom calculation method, investigates the grid generation approach appropriate for the calculation of near-field sonic boom, and the near-field calculation of typical cases.

The far-field sonic boom prediction approach based on the nonlinear Burgers equation and the sonic boom intensity evaluation standard are studied in detail in the fourth chapter. impact of waveforms.

The fifth chapter validates the result of near field and far field solution cases with data from sonic boom prediction workshop (SBPW1 and SBPW2).

The summary and prospect are covered in the sixth chapter. It both summarizes the research for this work and suggests areas for further research based on its limitations.

Chapter 2 Approach and Numerical Methods

It is possible to forecast the sonic boom characteristics in three steps, according to theory. The near-field static pressure signatures near the aircraft must be specified initially. The propagation of pressure signatures to the ground while taking nonlinear atmospheric turbulence into account is the second phase. Calculating the interactions between the boom signatures and the ground is the next stage. Figure 9 illustrates the process for predicting sonic booms.

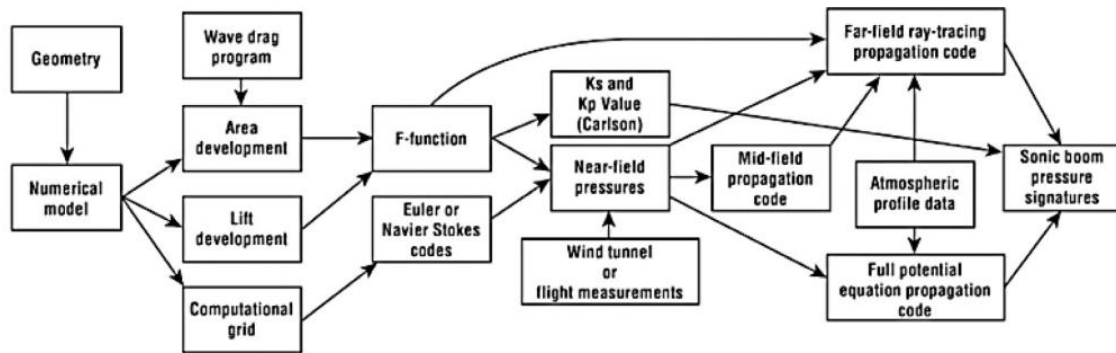


Figure 9 Ingredients of sonic boom prediction programs ^[5]

The parametric geometry model of the airplane serves as the starting point for the F-function technique. The geometry model is developed to have the necessary Mach number and azimuth angle. The aerodynamic analysis provides information on lift development. The resulting equivalent area distributions are fed into the Whitham^[7] F function to obtain the near-field signature, which develops into a ray-tracing code or a mid-field propagation program that more accurately takes into account nonlinear or three-dimensional phenomena. The output of the latter program is then sent into the propagation codes, which take atmospheric distortion into account to produce the precise ground-level sonic boom

characteristics. The K_s, K_p , and K_t factors are calculated using the Carlson methodology^[9,5] in a third route.

$$\Delta p_{\max} = K_p K_R \sqrt{p_v p_g} (M^2 - 1)^{1/8} h_e^{-3/4} l^{3/4} K_s \quad (2.1)$$

Bow-shock overpressure from the equation (2.1)

$$\Delta t = K_t \frac{3.42}{a_v} \frac{M}{(M^2 - 1)^{3/8}} h_e^{1/4} l^{3/4} K_s \quad (2.2)$$

And signature duration from the equation (2.2)

Table 1 Explanation of each parameter in formula (2.1) and formula (2.2)

Δp_{\max} is N-wave overpressure value	Δt is N-wave duration
K_p is a factor reflecting the overpressure value of the atmospheric influence	K_t is a factor reflecting the duration of the atmospheric influence
K_R is ground reflection factor	M is cruise Mach number
p_v is pressure at cruise altitude	h_e is effective cruising altitude
p_g is ground pressure	K_s is shape influence factor
l is fuselage length	a_v is speed of sound at cruise altitude

2.1 Nearfield CFD solution

A computational grid is the first step in the CFD technique. Since shock, jumps tend to smear as the distance from the configuration grows, the code should ideally feature an adaptive grid capacity to concentrate the grid near shocks or a shock fitting process. Since second order viscous effects apply to vehicles during cruise contexts, Euler equation codes are typically used. Numerous scholars have utilized the Euler equation to anticipate booms.

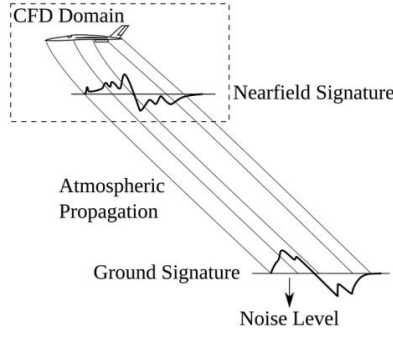


Figure 10 Sonic Boom prediction process^[13]

Inviscid Flow (the Euler Equations) is used for this simulation. Inviscid flow is, by definition, a flow where the dissipative, transport phenomena of viscosity, mass diffusion, and thermal conductivity are neglected. The equations for an unsteady, three-dimensional, compressible inviscid flow are displayed below^[14] in Eq.(2.3) to (2.5).

Continuity equation

Non-conservation form

$$\frac{D\rho}{Dt} + \rho \nabla \cdot V = 0 \quad (2.3)$$

Conservation form

$$\frac{\partial \rho}{\partial t} + \nabla \cdot (\rho V) = 0 \quad (2.4)$$

Momentum equation

Non-conservation form

$$\text{X component:} \quad \rho \frac{Du}{Dt} = -\frac{\partial p}{\partial x} + \rho \quad (2.5)$$

$$\text{Y component:} \quad \rho \frac{Dv}{Dt} = -\frac{\partial p}{\partial y} + \rho \quad (2.6)$$

$$\text{Z component:} \quad \rho \frac{Dw}{Dt} = -\frac{\partial \rho}{\partial z} + \rho \quad (2.7)$$

Conservation form

$$\text{X component:} \quad \frac{\partial(\rho u)}{\partial t} + \nabla \cdot (\rho u V) = -\frac{\partial \rho}{\partial x} + \rho \quad (2.5)$$

$$\text{Y component:} \quad \frac{\partial(\rho v)}{\partial t} + \nabla \cdot (\rho v V) = -\frac{\partial \rho}{\partial y} + \rho \quad (2.5)$$

$$\text{Z component:} \quad \frac{\partial(\rho w)}{\partial t} + \nabla \cdot (\rho w V) = -\frac{\partial \rho}{\partial z} + \rho \quad (2.5)$$

The inviscid Euler equation is used to solve the flow field, and its three-dimensional integral form^[15] is as shown in Eq.(2.6).

$$\frac{\partial}{\partial t} \int_{\Omega} Q dV + \oint_{\partial\Omega} F(Q) dS = 0 \quad (2.6)$$

Where, $Q=[\rho, \rho u, \rho v, \rho w, \rho E]^T$

is the conserved variable of the flow field, $F(Q)$ is the convective flux, and Ω is any grid unit. The equation is discretized in space using the finite volume method, and the Roe upwind method is used to calculate the convective flux at the interface of the control body. The flow field gradient is obtained by linear interpolation, and the Venkatakrishnan limiter is used to prevent new extremums from appearing; in the time direction, the backward difference implicit scheme is used to discretize, and the obtained discretization equation^[15] can be expressed as:

$$\left(\frac{V}{\Delta t} I + \frac{\partial R}{\partial Q} \right) \Delta Q + R(Q) = 0 \quad (2.7)$$

$$\text{Where, } R(Q)_i = \sum_{j=1}^{\text{Neighbors}} F_{ij} \cdot \Delta S$$

is the flow field residual. The discretized equations are solved iteratively with the GMRES method, and after convergence, R tends to at zero. For the detailed flow field solution method, please refer to ^[15].

Commercial CFD software is used in the study of nearfield CFD. Commercial CFD software was chosen for CFD solution because it has a more user-friendly interface and workflow, better meshing, parallel performance and scalability, more physics models and solvers, and more post-processing and visualization options. The Commercial CFD software used in this study is also a very powerful software package that is widely used in industry and academia.

For finding the dp/p_{inf} we use the following formula^[15] in Eq.(2.8).

$$\frac{dp}{p_{inf}} = \frac{p_{inf} - p_{absolute}}{p_{inf}} \quad (2.8)$$

Where, $p_{inf} = 101325$ Pa & $p_{absolute}$ is the absolute pressure measured in the data extraction after CFD calculation. To get the nearfield plot this dp/p_{inf} is plotted against distance on X-axis (m).

2.2 Far field solution

A far field propagation tool should have a time domain algorithm to account for all the propagation mechanisms with more extensions. The first addition is the capacity to handle various input waveforms, including an off body dp/p pressure waveform, F function derived, possibly from the boom minimization theory, or an equivalent area distribution utilized in design exercises. Predicting ground signatures in the presence of wind profiles that are horizontally stratified is the second extension. The capability to operate in unusual environments is the third extension. Users may supply distributions of the temperature,

wind, and relative humidity in this instance. The fourth extension is offtrack signature prediction. The prediction of the location of the ground intersection with regard to the aircraft location is the fifth extension. These are the extensions used by sBoom^[12].

$$\frac{\partial p}{\partial x} = \frac{\beta p}{\rho_0 c_0^3} \frac{\partial p}{\partial t'} + \frac{\partial}{2c_0^3} \frac{\partial^2 p}{\partial t'^2} + \sum_v \frac{c'_v}{c_0^2} \int_{-\infty}^t \frac{\partial^2 p}{\partial y^2} e^{-(t'-y)/t_v} dy \quad (2.9)$$

Given in Eq. (2.9), the Burgers equation takes into account a variety of molecular relaxation phenomena, including nonlinearity, thermos-viscous absorption, and more, as vibrations travel through the atmosphere. As seen in Eq. (2.10), this equation can be transformed into without dimensions representation with the addition of new factors due to geometrical dispersion and transmission across a stratified atmosphere^[12]

$$\frac{\partial P}{\partial \sigma} = P \frac{\partial P}{\partial \tau} + \frac{1}{\Gamma} \frac{\partial^2 P}{\partial \tau^2} + \sum_v C_v \frac{\frac{\partial^2}{\partial \tau^2}}{1 + \theta_v(\partial/\partial \tau)} P - \frac{\frac{\partial A}{\partial A}}{2A} P + \frac{[\partial(\rho_0 c_0)/\partial \sigma]}{2\rho_0 c_0} P \quad (2.10)$$

bBoom far field propagation tool is used to propagate the nearfield solution, Which is a similar program working on burger equations. It requires the extracted data of nearfield solution.

2.3 Post processing and verification

Post processing software is used for plotting the graph and exporting the image files used in this paper. The nearfield solution and far field solution obtained from the cfd solution and far field propagation tool was compared with the data at last using the post processing software.

Chapter 3 Nearfield solution

For this study two geometries were selected each from SBPW1 and SBPW2. They are Delta-Wing-Body(DWB) and JAXA-Wing-Body(JWB). CFD software was used for meshing and solving the nearfield solution because it applies the finite volume method as a discretization scheme. Euler equations is used to solve Compressible and inviscid flow. It is a steady simulation. Coupled style relation between pressure field and velocity field is used. For DWB, the simulation was carried out to match the wind tunnel experimental data using normal sea level temperature and pressure while for the JWB, the simulation was carried out to match the cruise altitude of this aircraft.

3.1 69° Delta-Wing-Body (DWB)

A replica wind tunnel built to study sonic boom was used in a 1973 wind tunnel experiment.^[17] The experiment was conducted in a 9 by 7-foot supersonic wind tunnel at the NASA Ames Research Center. A schematic of the wind tunnel setup may be seen in Figure 12.

Two pressure probes affixed to the wind tunnel wall were used to measure the near-field signature. Four pressure orifices were spaced out along the exterior of each probe. Orifices for the reference probe were placed in a plane normal to the free stream, while those for the overpressure probe were situated in a plane parallel to the Mach angle. This arrangement yields a more recognizable signature.^[17]

Originally referred as "Model 4" by Hunton, Hicks, and Mendoza^[17] in 1973. Figure 11 illustrates this geometry from several viewpoints, including planform, side, and sectional views. The model is an analytically determined tangent-ogive-cylinder on a steep delta-wing with a 5% thick diamond cross section. This geometry has been the subject of several

computational studies, and one of its forms was examined at the NASA Fundamental Aeronautics Workshop in 2008. ^[18].

3.1.1 DWB: Geometry

The DWB model has fuselage length of 6.9 inches from nose to base. As illustrated in the inset of Figure 11, the delta wing has a maximum span of 2.72 inches and a leading edge that is swept 69 degrees with a 5% thick diamond cross section. The workshop provided the geometry. The solid model in igs file format had a Boolean bug when it was subtracted using origin as symmetry plane.

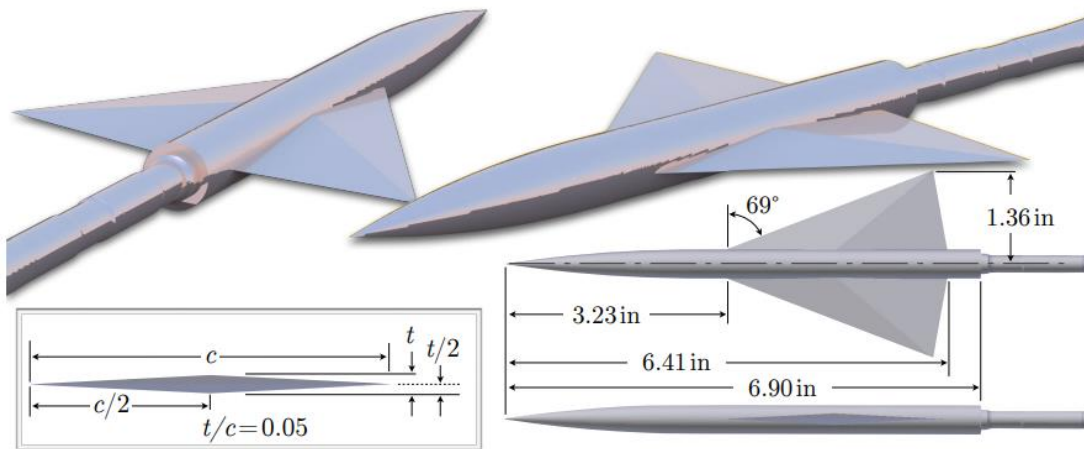


Figure 11 69° Delta Wing-Body different views^[18]

To fix this bug the model was extruded a little along the negative y-direction, which fixed the bug. Moreover, the model support part behind the actual geometry was removed using the Boolean function to reduce the mesh size and calculation burden, as it is not necessary for the shock wave prediction in numerical analysis.

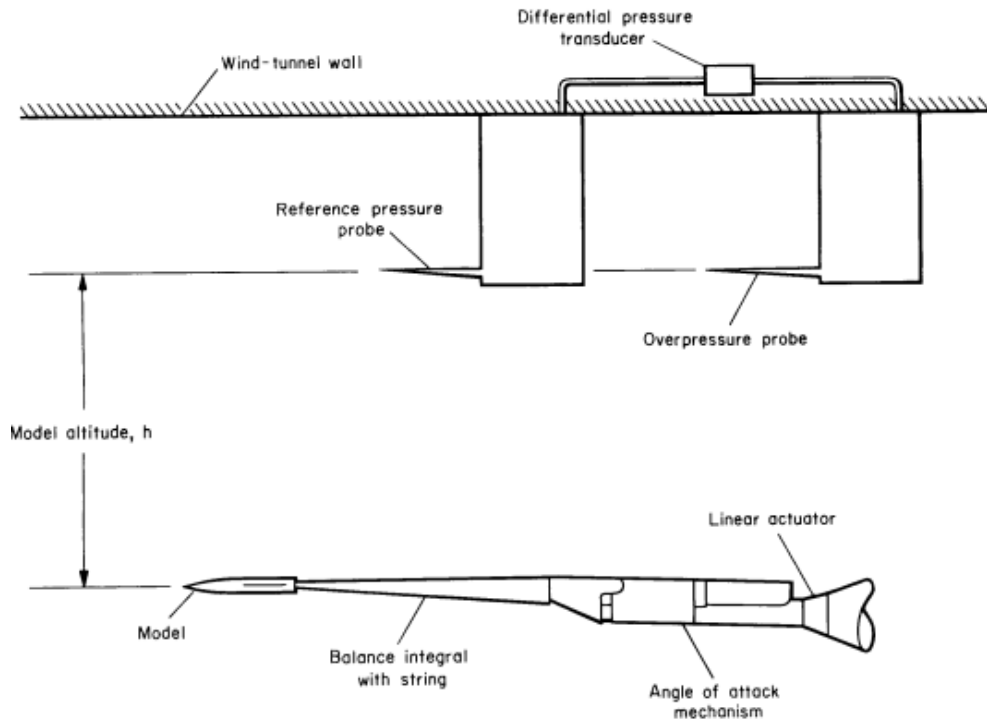


Figure 12 Wind-tunnel Apparatus Sketch^[17]

3.1.2 DWB: Meshing

The meshing is done in two step, firstly an initial mesh is calculated using the meshing tool in CFD software to get the general solution that captures the necessary flow pattern to capture the final solution phenomena. Secondly, this initial mesh was used for adaptive mesh as a reference mesh and was extended more using mesh refinement criteria later on. Cartesian coordinate system is applied in grid system. Surface remesher and trimmer cell mesher is used which is Cartesian 3D grid. The grid lines are tilted by using different coordinate system for meshing with angle of 35° with respect to lab reference frame or initial co-ordinate system.

3.1.2.1 Initial meshing

Custom Volumes control extending below the geometry were used to provide more cells for the important region where there is more likely to occur shock wave phenomenon. After various trials of appropriate mesh generation, this initial mesh was found to capture the general flow and shock wave pattern. Figure 13 shows the full domain of the mesh generation in parallel Z-X and perspective view. Figure 14 shows more detail in the mesh and Figure 15 shows the line of data extraction for finding the nearfield pressure signature in post processing software while Figure 16 gives the surface mesh view on DWB.

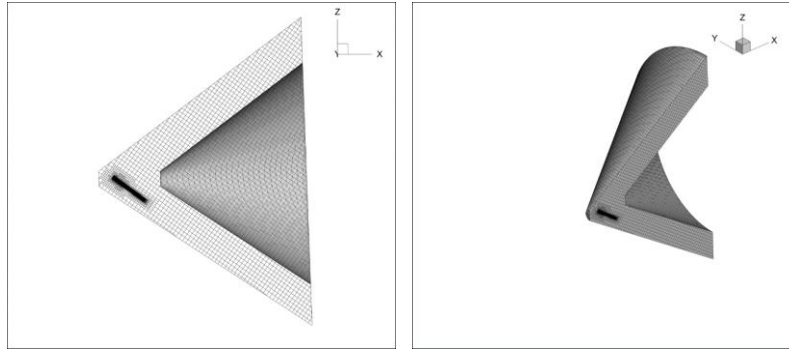


Figure 13 Initial Mesh Domain around the 69° Delta Wing-Body without support structure

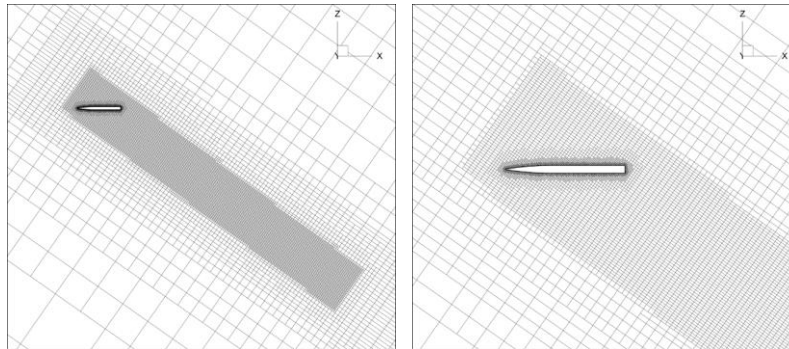


Figure 14 Initial Mesh Zoomed view around the 69° Delta Wing-Body without support structure

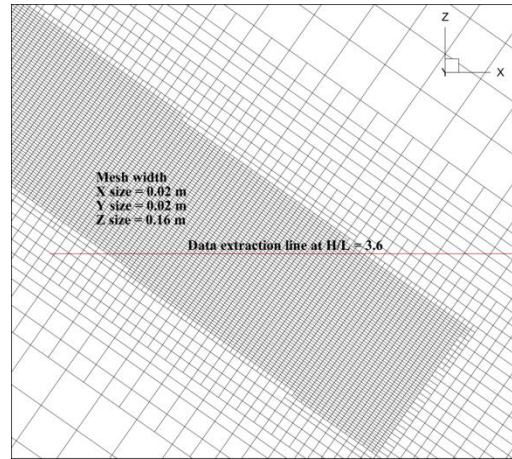


Figure 15 Initial mesh minimum width of 0.02m & data extraction at $H/L=3.6$

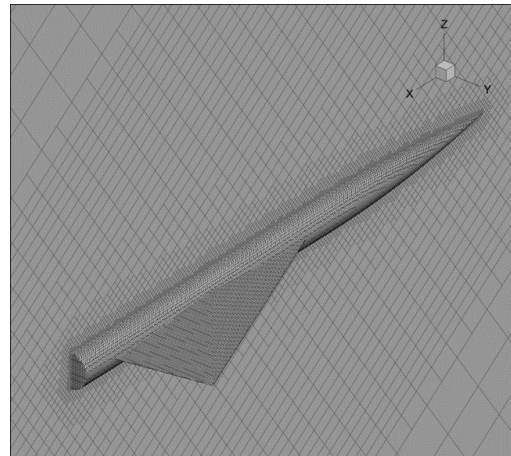


Figure 16 Initial mesh on DWB surface

Table 2 DWB Initial mesh cell count

Types of cells	Number of cells
Tetrahedral	4397
Hexahedral	258357
Wedge	9580
Pyramid	26
Polyhedral	45248
Total	317608
Halo cells	40383

Halo cells are cells shared for parallel processing. Initial mesh has 958286 faces (23479 triangular, 909603 quadrilateral and 53056 polygonal) 27852 halo faces and 372040 vertices (31182 halo vertices).

3.1.2.2 Adaptive final mesh

The Mach gradient or gradient of Mach number times adaptive cell size as shown in Eq. (3.1) was used as an adaptive mesh criteria with 2 levels of refinement. Figure 17 shows the domain while Figure 18 gives the zoom view on final mesh. In addition, Figure 19 shows the line of data extraction for finding the nearfield pressure signature in post processing software while Figure 20 gives the surface mesh view on DWB final mesh.

$$\text{adaptive mesh criteria} = \text{Gradient of mach number} \times \text{adaptive cell size} \quad (3.1)$$

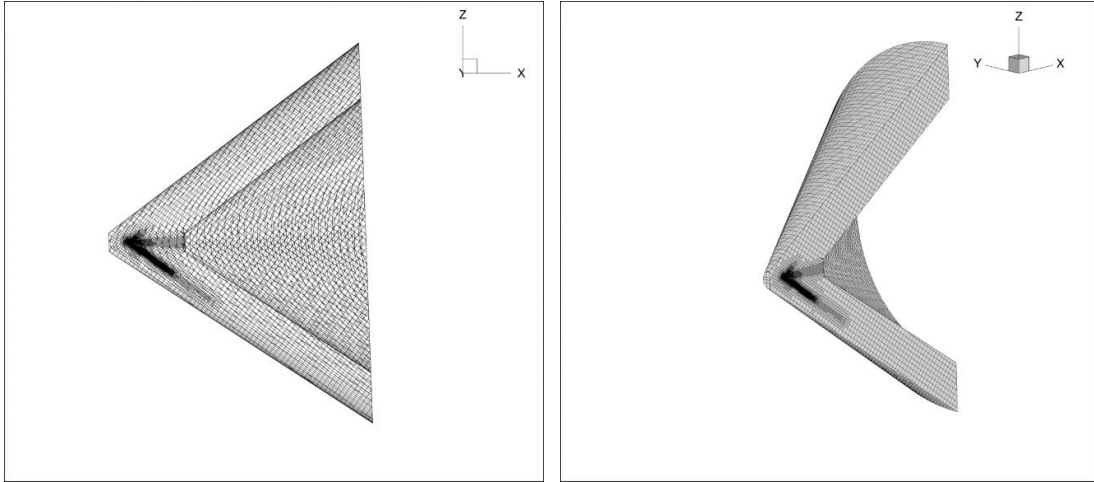


Figure 17 Final Mesh Domain around the 69° Delta Wing-Body without support structure

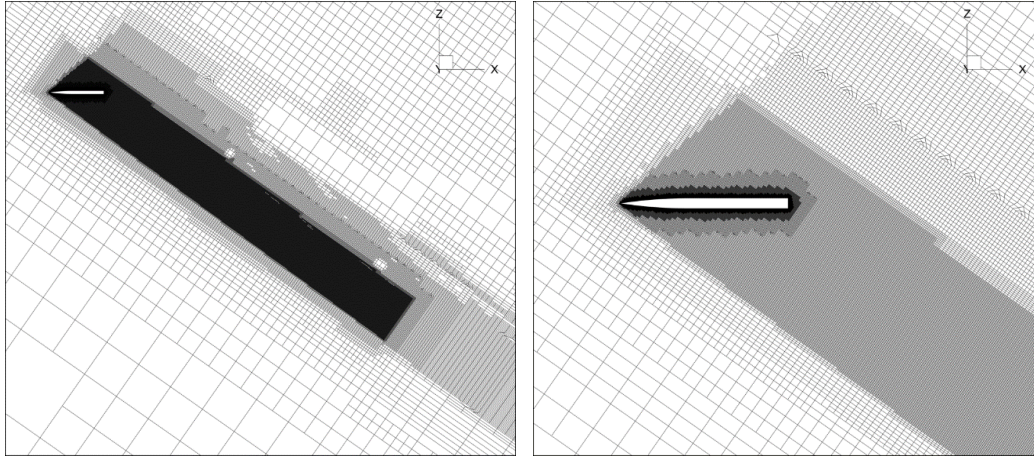


Figure 18 Final Mesh Zoomed view around the 69° Delta Wing-Body without support structure

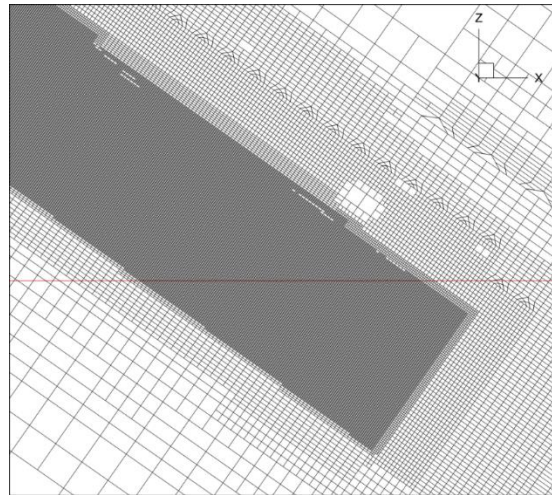


Figure 19 Final mesh minimum width of 0.001m and data extraction at $H/L=3.6$

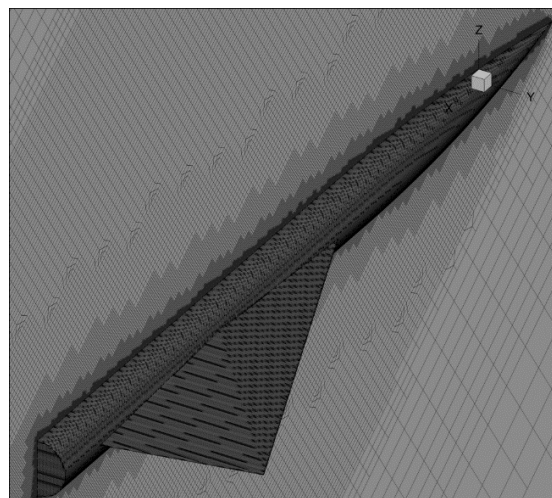


Figure 20 Final mesh on DWB surface

Table 3 DWB final mesh cell count

Types of cells	Number of cells
Tetrahedral	1020
Hexahedral	13481998
Wedge	2713
Pyramid	11
Polyhedral	289929
Total	13775671
Halo cells	480090

DWB final mesh has 41348728 interior faces (5773 triangular, 41291338 quadrilateral, 360479 polygonal) (308862 halo faces) and 14361068 vertices (319383 halo vertices)

3.1.3 DWB: CFD Solution

The region has three boundaries freestream, wall and symmetry plane. The outside domain is defined as freestream type boundary and freestream velocity is $1.7 \times 340 \text{ m/s} = 578 \text{ m/s}$ in +ve x-direction. The model surface is defined as wall boundary. Plane of symmetry is defined as symmetry boundary. Inviscid viscous regime was used.

AMD Ryzen Threadripper 2990WX 32-Core processor 3.00 gigahertz (GHz) max speed with 128 gigabytes (GB) RAM was used for this simulation. The simulation took less than an hour to obtain a converged state.

As the simulation progresses towards a convergent solution, adaptive mesh was used after 300 steps and in each 5 steps the mesh was adapted to get a grid convergence and better solution in sonic boom propagation areas.

For this gradient of Mach number times adaption cell size was used adaptive mesh criteria. Refinement adaption operation of cell field function value above the range upper limit while the value in between is kept as it is and below is coarsened. The simulation is stopped when the solution reaches the converged state and grid convergence is achieved. Converged CFD result can be seen as the pressure contours shown with data extraction line at height of 0.63m necessary for nearfield solution calculation in Figure 21 and 22 while Figure 23 gives the pressure contours on surface the surface of the DWB model.

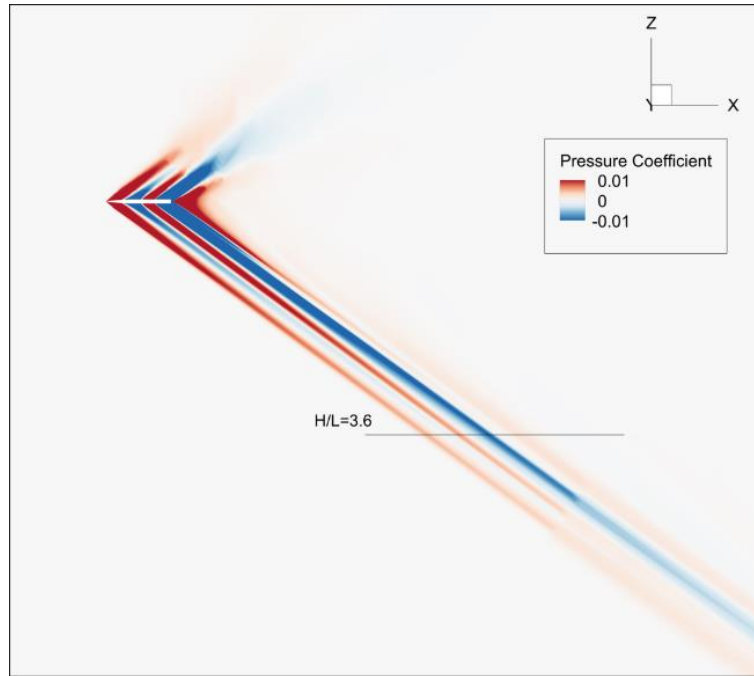


Figure 21 69° Delta Wing-Body Mach Line Contours on Pressure coefficient (C_p), Initial mesh, $Mach = 1.7$, $\alpha = 0^\circ$, $\phi = 0$, Inviscid solution showing the data extraction line at $H/L = 3.6$

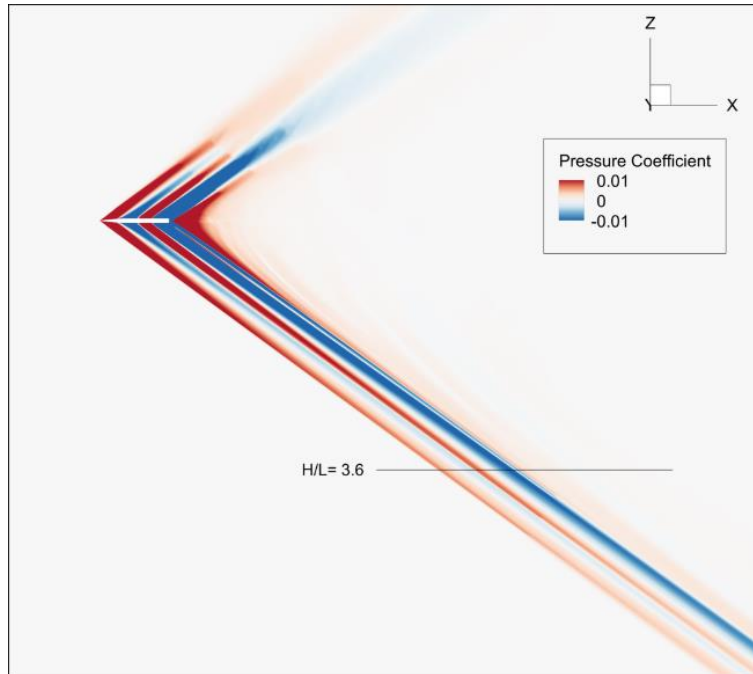


Figure 22 69° Delta Wing-Body Mach Line Contours on Pressure coefficient(C_p), final mesh, $Mach = 1.7$, $\alpha = 0^\circ$, $\phi=0$, Inviscid solution showing the data extraction line at $H/L= 3.6$

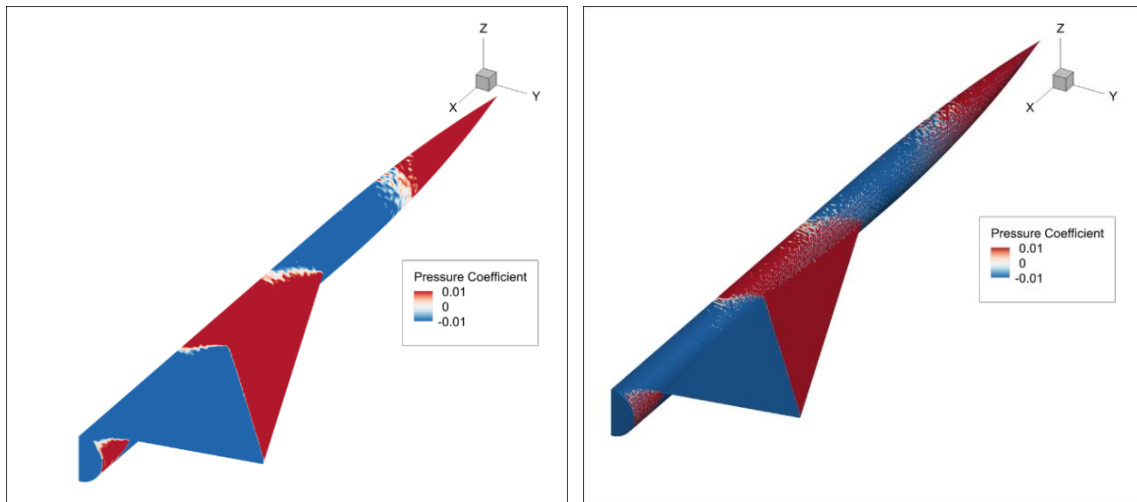


Figure 23 69° Delta Wing-Body surface Contours on Pressure coefficient (C_p) , Initial & Final mesh, $Mach = 1.7$, $\alpha = 0^\circ$, $\phi=0$, Inviscid solution

3.1.4 DWB: Nearfield solution

The near field solution on dp/p_{inf} to $X(m)$ plot can be seen in Figure 24. Obviously, the final mesh has solution that is more accurate. Therefore, the final mesh solution is the actual solution while initial mesh is shown for comparison with the final mesh.

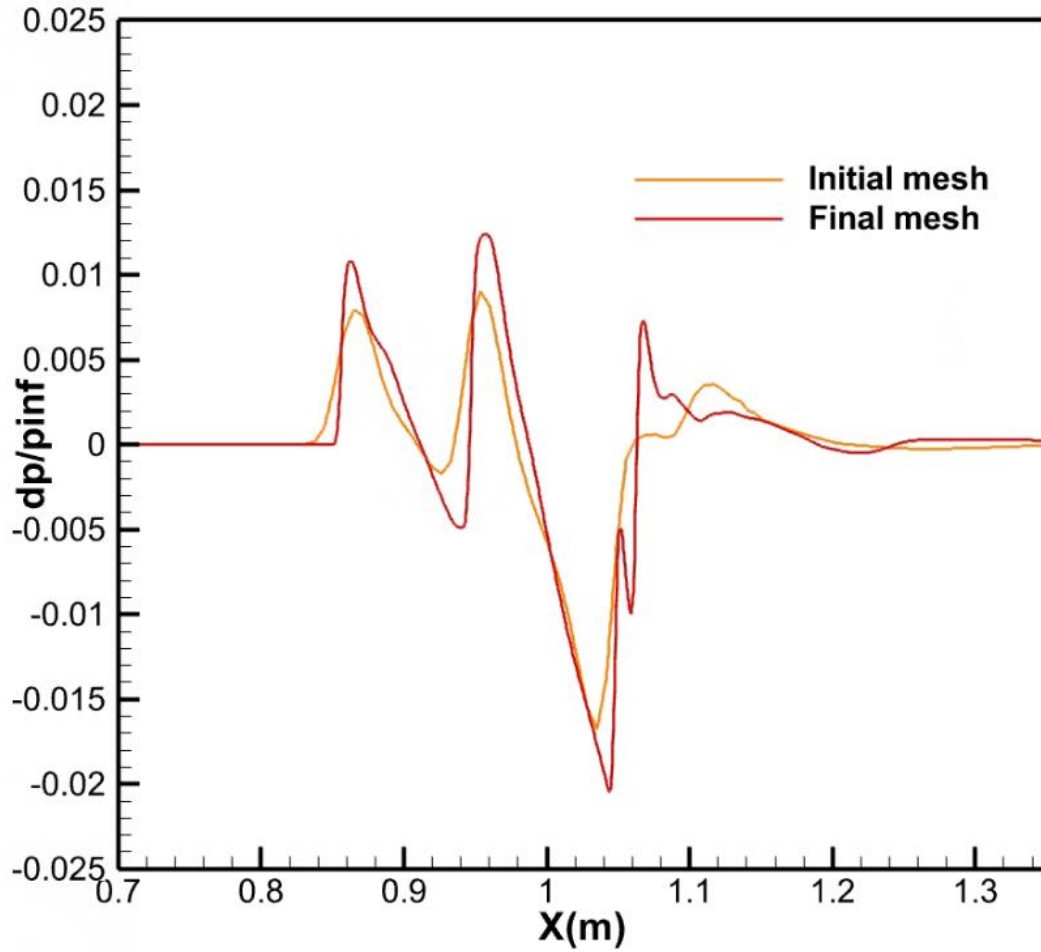


Figure 24 Final adaptive mesh and initial mesh Pressure distribution (dp/p_{inf})

comparison of 69° Delta Wing, : $M=1.7, \alpha=0^\circ, \phi=0$ at $H/L= 3.6$

3.1.5 DWB: Near field comparison with SBPW1

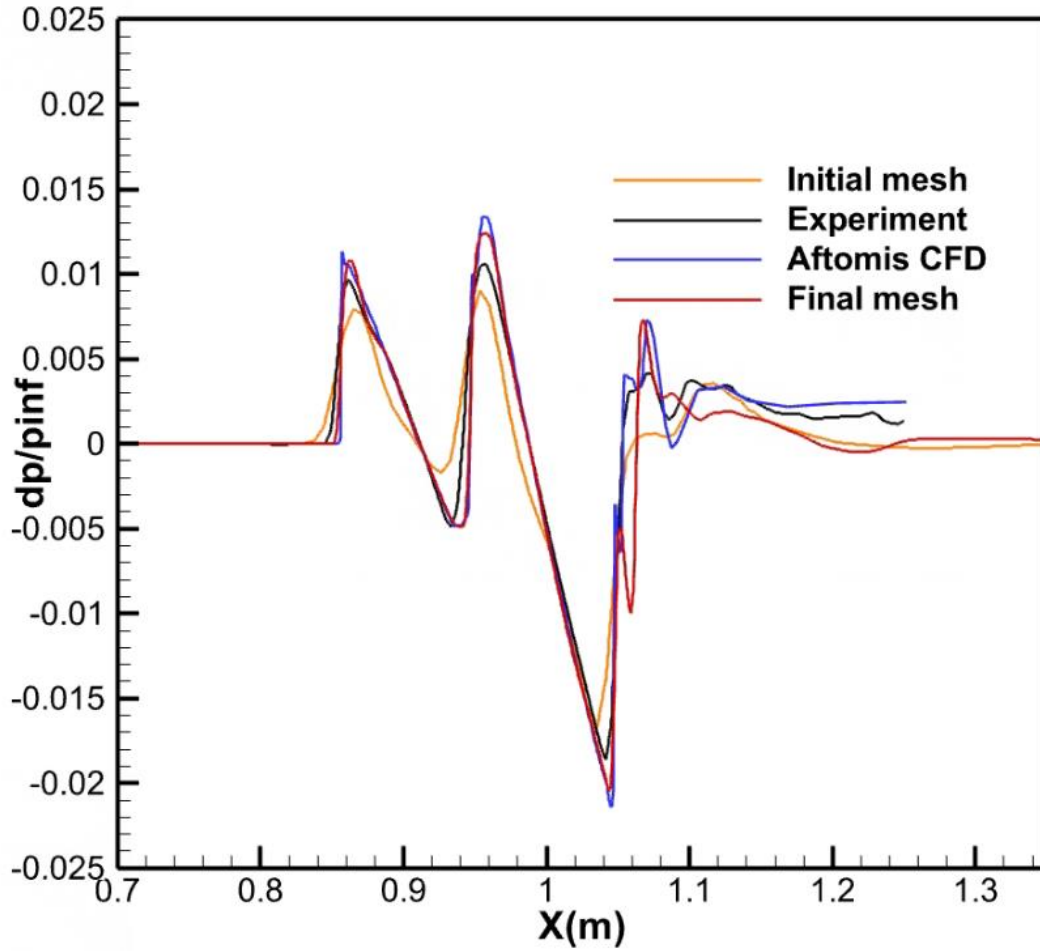


Figure 25 All Pressure distribution (dp/p_{inf}) comparison of 69° Delta Wing, CFD vs.

Experiment: $M=1.7, \alpha=0^\circ, \phi=0$ at $H/L=3.6$

In Figure 25, the initial sudden increase of pressure means a shock wave of airplane head. The orange line is smoother instead of sudden increase, which means the simulated shock wave is dissipated in coarser mesh. While for final mesh, the red line, the simulated shock wave is sharp and better. The peak of near field wave, for coarser/initial mesh, is much lower, which is not very good and does not match the Aftomis CFD and experiment result

very well but the final mesh is able to capture the shock wave and is able to better match the Aftomis CFD as well as experiment from first sonic boom prediction workshop.

3.2 JAXA Wing Body(JWB)

The NASA Concept 25D's equivalent area target was used in the design of the JWB, a wing-body configuration. To match the equivalent area target, the first stage of the design included inviscid simulation and form optimization. Reverse equivalent area based optimization, inviscid flow, and multipole analysis were applied in the second phase.

3.2.1 JWB: Geometry

The JWB design process is described by Ueno, Kanamori, and Makino^[19]. The JWB shown in Figure 26 is a wing body configuration designed to the same equivalent area target as the NASA Concept 25D^[20]. To match the equivalent area target at the initial stage of the design, Euler calculations and form optimization were used. Reversed equivalent area-based optimization using Euler and multipole analysis was employed in the second phase. In order to disrupt the shock wave at the rear fuselage, this JWB layout features a significant expansion around the lower fuselage closeout. For RANS models, the specifics of this powerful expansion and how it interacts with the back fuselage shock are very different. CATIA exported the body and wing geometry as IGES surfaces. These surfaces were integrated into a solid model and rotated to account for the 2.3067° design angle of attack^[21].



Figure 26 Rendering of the supersonic low-boom JAXA Wing Body geometry^[22]

A 38.7 m body length and extraction points of 0.85 and 2.55 body lengths at off-track angles of 0° , 10° , 20° , 30° , 40° , and 50° were mentioned in the original issue description. The body length employed in this study is 38.7 m, and the extraction location is 2.55 body lengths as shown in Figure 30. In addition, at the off track angle of 0° is calculated.

3.2.2 JWB: Meshing

Similar to the DWB the meshing is done in two step, first an initial mesh shown in Figure 27-30 is calculated using the meshing tool in CFD software to get the general solution that is able to capture the necessary flow pattern required for final mesh as shown in Figure 31-34. Secondly, this initial mesh was used for adaptive mesh as a reference mesh and was extended more using mesh refinement criteria later on. Cartesian coordinate system is applied in grid system. Surface remesher and trimmer cell mesher is used which is Cartesian 3D grid. The grid lines are tilted by using different coordinate system for meshing with angle of 35° with respect to lab reference frame or initial co-ordinate system.

3.2.2.1 Initial meshing

Custom Volumes control extending below the geometry were used to provide more cells for the important region where there is more likely to occur shock wave phenomenon.. After various trials of appropriate mesh generation, this initial mesh was found to capture

the general flow and shock wave pattern. Figure 27 shows the full domain of the mesh generation in parallel Z-X and perspective view. Figure 28 shows more detail in the mesh while Figure 29 gives the surface mesh view on JWB. Figure 30 shows the data extraction line and cell size in the data extraction location.

Table 4 JWB Initial mesh cell count

Types of cells	Number of cells
Tetrahedral	7312
Hexahedral	2945086
Wedge	9306
Pyramid	144
Polyhedral	1463
Total	3108200
Halo	260389

JWB Initial mesh has 9378678 interior faces (34618 triangular, 9349491 quadrilateral, 181038 polygonal) (186469 halo faces) and 3269152 vertices (193007 halo vertices)

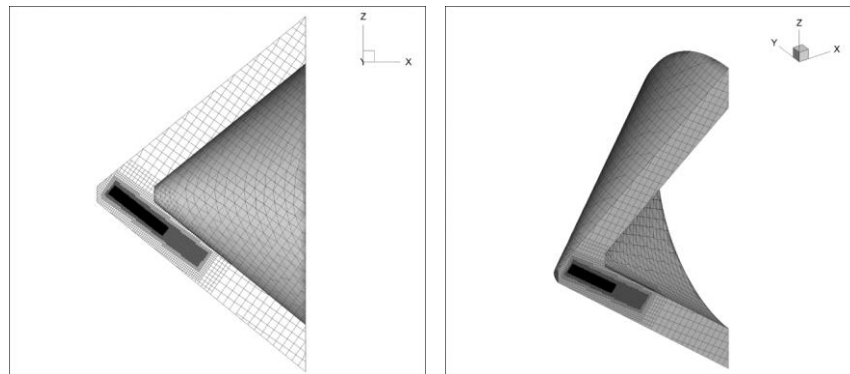


Figure 27 Initial Mesh Domain around the JAXA Wing-Body without support structure

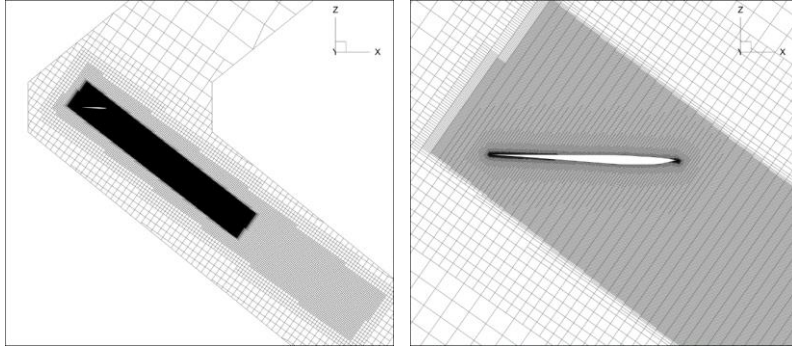


Figure 28 Initial Mesh Zoomed view around the JAXA Wing-Body

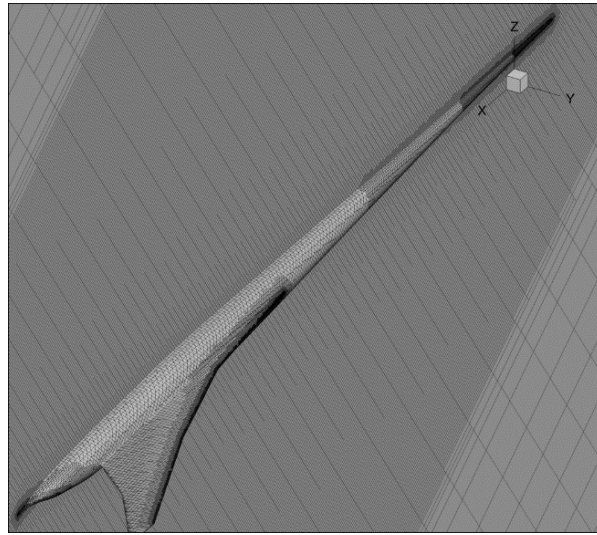


Figure 29 Initial mesh on JWB surface

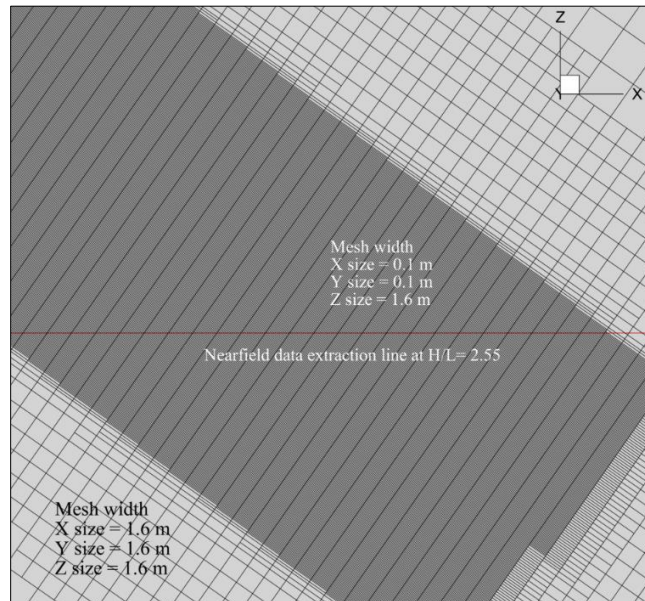


Figure 30 Initial mesh minimum mesh width of 0.1m & data extraction at 2.55

3.2.2.2 Adaptive final mesh

The Mach gradient or gradient of mach number was used as an adaptive mesh criteria with 1 levels of refinement. The Figures below shows the final adaptive meshes Figure 31 shows the domain while Figure 32 gives the zoom view on final mesh and Figure 33 shows the final mesh on JWB surface. Figure 34 shows the data extraction line and cell size in the data extraction location.

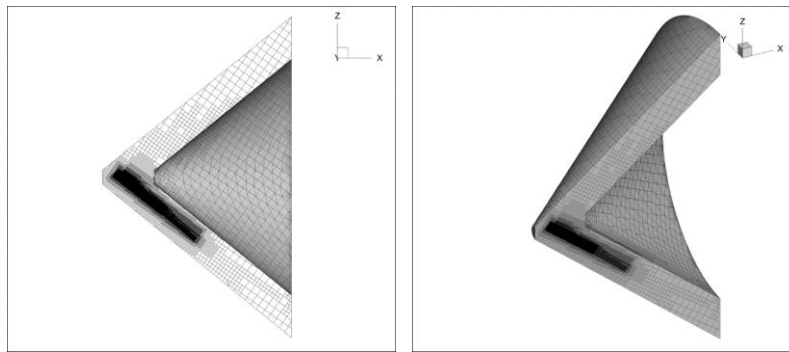


Figure 31 Final Mesh Domain around the JAXA Wing-Body

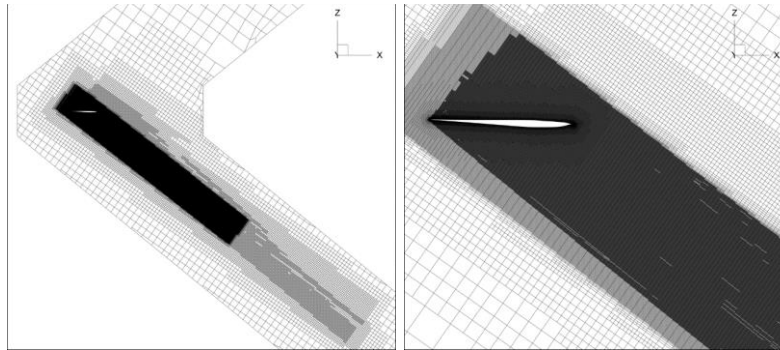


Figure 32 Final Mesh Zoomed view around the JAXA Wing-Body

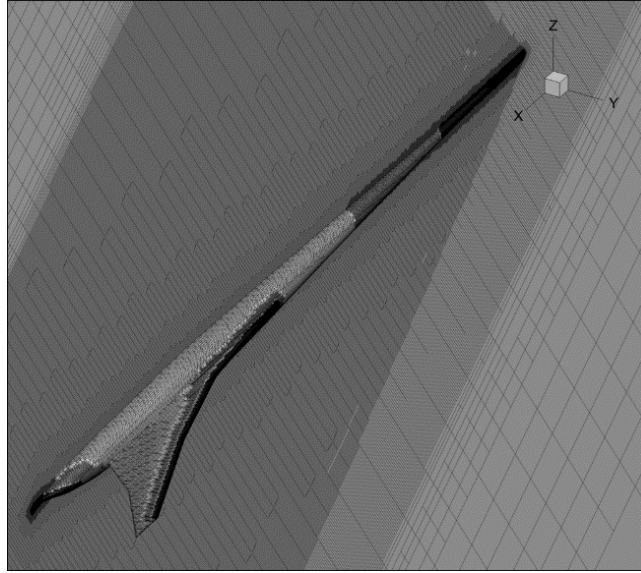


Figure 33 Final mesh on JWB surface

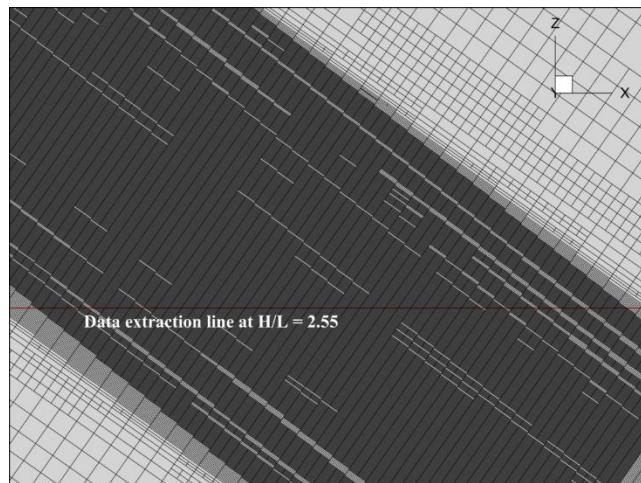


Figure 34 Final mesh minimum mesh width at data extraction of 0.05 m

Table 5 JWB final mesh cell count

Types of cells	Number of cells
Tetrahedral	389
Hexahedral	21076487
Wedge	709
Pyramid	7
Polyhedral	409351
Total	21486943
Halo	924572

JWB Final mesh has 64855966 interior faces (2565 triangular, 64954695 quadrilateral, 544028 polygonal) (645322 halo faces) and 22224094 vertices (664562 halo vertices)

3.2.3 JWB: CFD Solution

The region has three boundaries freestream, wall and symmetry plane. The outside domain is defined as freestream type boundary and freestream velocity is 1.6×295.375 m/s (speed of sound at an altitude of 15500 m) = 472.6 m/s in +ve x-direction. The model surface is defined as wall boundary. Plane of symmetry is defined as symmetrical boundary.

AMD Ryzen Threadripper 2990WX 32-Core processor 3.00 gigahertz (GHz) speed with 128gigabytes (GB) RAM was used for this simulation. The initial simulation took less than an hour to obtain a converged state while the final mesh took 6-8 hours to get to an converged state.

As the simulation progresses towards a convergent solution, adaptive mesh was used after 500 steps and in each 100 steps the mesh was adapted to get a grid convergence and better solution in sonic boom propagation areas. For this gradient of Mach number times adaption cell size was used as adaptive mesh criteria.

Refinement adaption operation of cell field function value above the range upper limit while the value in between is kept as it is and below is coarsened. The simulation is stopped when the solution reaches the converged state and grid convergence is achieved.

Converged CFD result can be seen as the pressure contours shown with data extraction line at height of 98.7 m necessary for nearfield solution calculation in Figure 35&36 while Figure 37 gives the pressure contours on surface the surface of the JWB model comparison on initial and final mesh.

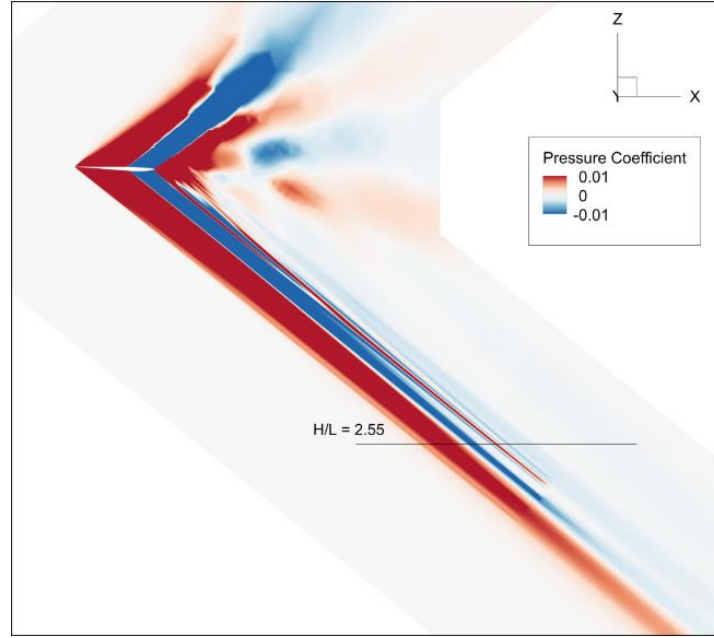


Figure 35 JAXA Wing-Body Mach Line Contours on Pressure coefficient(C_p), initial mesh, $Mach=1.6$, $\alpha=0^\circ$, $\phi=0^\circ$, Inviscid solution showing the data extraction line at $H/L=2.55$

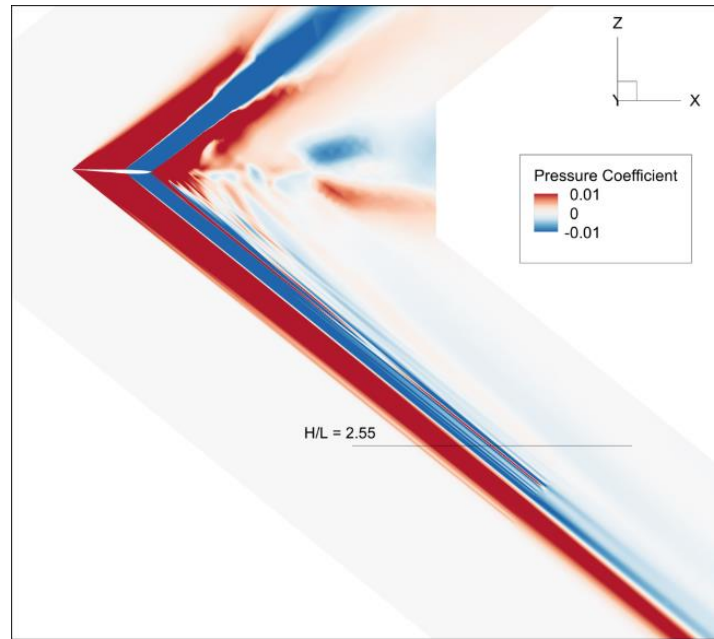


Figure 36 JAXA Wing-Body Mach Line Contours on Pressure coefficient(C_p), final mesh, $Mach=1.6$, $\alpha=0^\circ$, $\phi=0^\circ$, Inviscid solution showing the data extraction line at $H/L=2.55$

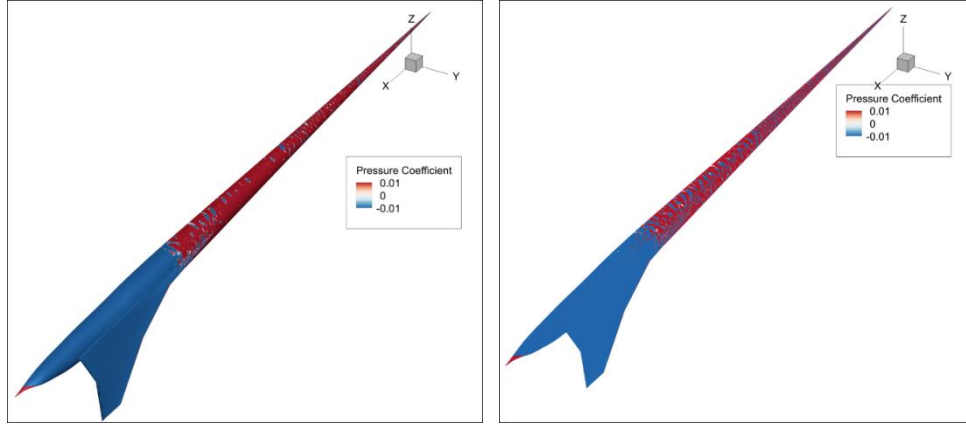


Figure 37 JAXA Wing-Body surface Contours on Pressure coefficient(C_p) , initial mesh& Final mesh, $Mach = 1.6$, $\alpha = 0^\circ$, $\phi=0^\circ$, Inviscid solution

3.2.4 JWB: Nearfield solution

The near field solution of JWB on dp/p_{inf} to $X(m)$ plot can be seen in Figure 38. Obviously, the final mesh has solution that is more accurate. Therefore, the final mesh solution is the actual solution while initial mesh is shown for comparison.

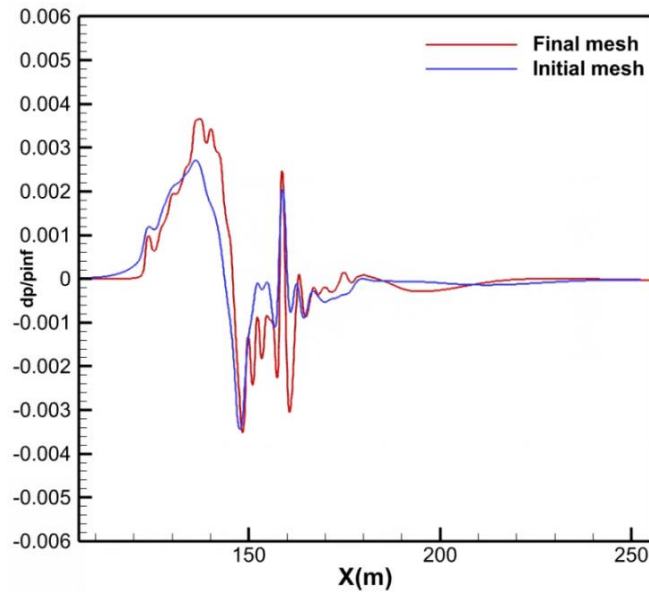


Figure 38 Final adaptive mesh and initial mesh Pressure distribution (dp/p_{inf}) comparison of JAXA Wing, $M=1.6$, $\alpha=0^\circ$, $\phi=0^\circ$ at $H/L= 2.55$

3.2.5 JWB: Near field comparison with SBPW2

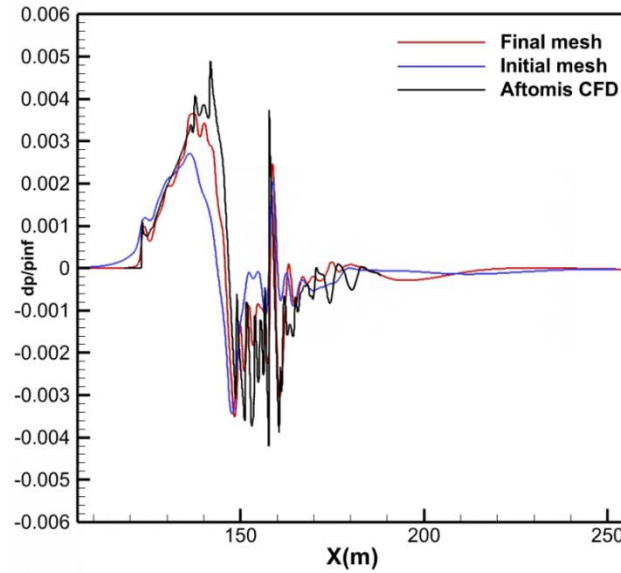


Figure 39 All Pressure distribution (dp/p_{inf}) comparison of JAXA Wing, My CFD vs.

SBPW2: $M=1.6, \alpha=0^\circ, \phi=0^\circ$ at $H/L=2.55$

The quick increase in pressure indicates an airplane head shock wave in Figure 39. The blue line here is smoother rather than abruptly increasing; indicating that the simulated shock wave has been significantly diffused in the coarser mesh. The simulated shock wave is sharper and better for the final mesh, as seen by the red line. The peak of the near field wave is considerably lower for coarser/initial mesh, which is not ideal, but the final mesh captures the shock wave better and is able to better match the Aftomis CFD from second sonic boom prediction workshop.

Chapter 4 Far field solution

bBoom far field propagation tool^[23,24] is used to find the ground signature while the input signal are the near field solution calculated earlier using the CFD software. The data extraction were done at $H/L = 3.6$ for DWB and 2.55 for JWB using post processing software.

4.1 DWB: Ground propagation

The DWB model was applied to the research of pressure signal modeling in the first Sonic Boom Prediction Workshop. $Ma = 1.7$, $\alpha = 0^\circ$.

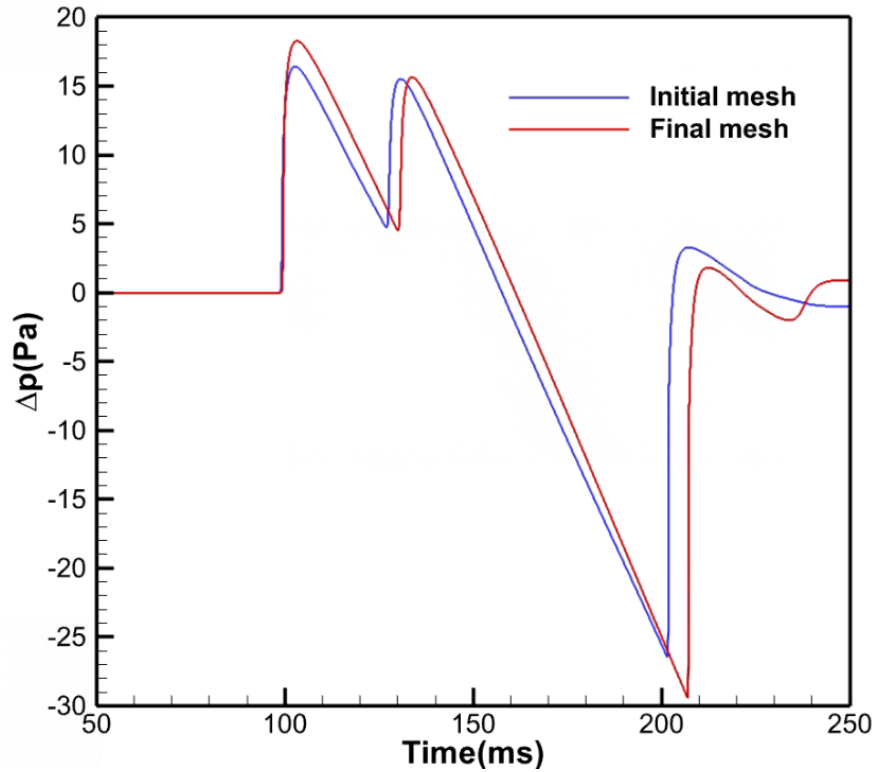


Figure 40 Final adaptive mesh and initial mesh Ground signature comparison of 69°Delta Wing, : $M=1.7, \alpha=0^\circ, \phi=0^\circ$ at an altitude of 16764m(55000 ft)

For the far field propagation of DWB model, it was rescaled from the model length 0.17526m used in the simulation to the actual aircraft size by dividing with 0.0065(from SBPW1 sBoom file) which turned out to be 26.96m and it was propagated from an altitude of 16764m to the ground with reflection factor of 1.9. The far-field sonic boom waveform and PL sound pressure level were calculated.

The loudness in initial mesh of DWB was 94.89 PLdB while it was 95.68 PLdB in final mesh. From Figure 40 we can see that the pressure distribution has increased on the same time interval, which has influenced the increase in loudness later for the adaptive mesh. Final mesh has more cells to better capture the flow and is more accurate than the initial mesh. Initial mesh was not able to capture this while the adaptive mesh with more cells clearly has more solution and was able to capture this is why the loudness has increased and the graph is bigger and shifted more over time.

4.2 DWB: Far field comparison with SBPW1

The time axis of the ground signatures have been shifted so that all the initial pressure rises occur at 100 ms. The large variation in overshoots and undershoots and the complex signature due the base flow seen in the near field have been filtered by the propagation process. Figure 41 compares the initial mesh and final mesh far field solution with Sonic boom prediction workshop 1 (Aftomis CFD). We can see that the solution in initial mesh is close but lower pressure falls below the Aftomis CFD, the final mesh is more accurate and is matching with the first sonic boom prediction workshop data(Aftomis CFD). The location of the middle and after-shocks show more variation than the expansion slopes. This change in shock positions results in different minimum and maximum pressures of the main expansion.

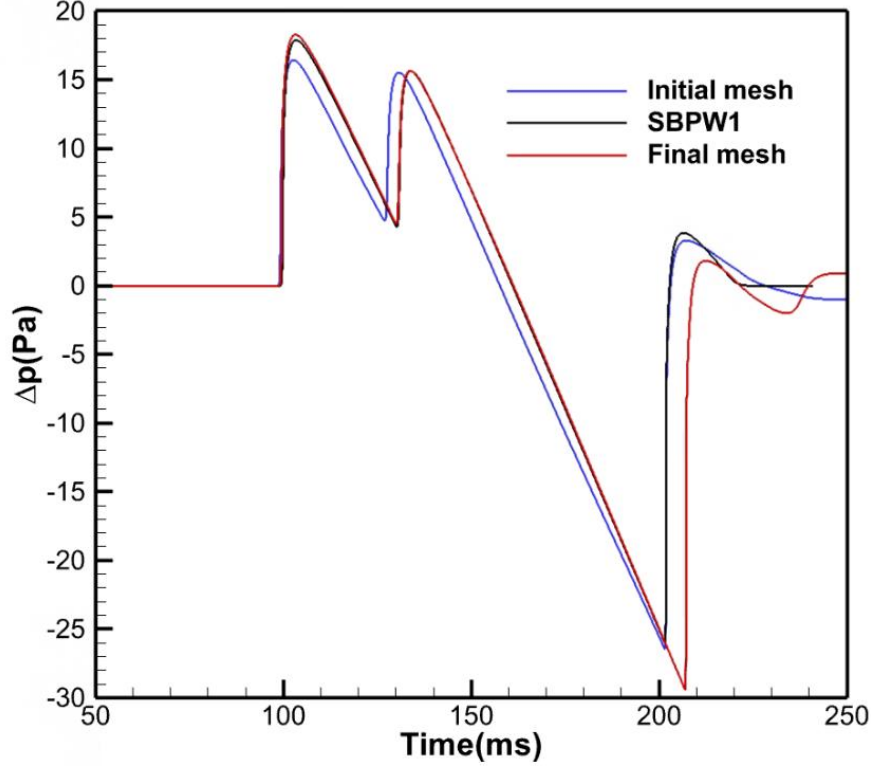


Figure 41 Final adaptive mesh Ground signature comparison of 69° Delta Wing, My CFD vs. SBPW1 (Aftomis CFD): $M=1.7, \alpha=0^\circ, \phi=0^\circ$ at $H/L=3.6$

4.3 JWB: Ground Propagation

The JWB model was used in the research of pressure signal modeling in the second Sonic Boom Prediction Workshop. $Ma = 1.6$, $\alpha = 2.3067^\circ$ (even though the incoming flow angle of attack is 0° , the model has a downward deflection of 2.3067° around the nose), and the cruising altitude of 15.76 km are the near-field simulation settings.

In this paper, the near-field sonic boom signal calculated earlier by using CFD software is used as the input to the far-field propagation program bBoom, whose near-field simulations are computed inviscidly using mesh adaptation techniques. Under standard atmospheric conditions, the near-field sonic boom signals at $\phi=0^\circ$ off-track angle, the signal propagates from the cruising altitude to the ground, and the ground reflection factor is taken as 1.9.

The calculated far-field sonic boom waveform and PL sound pressure level. The results of the bBOOM program is shown in Figure 42.

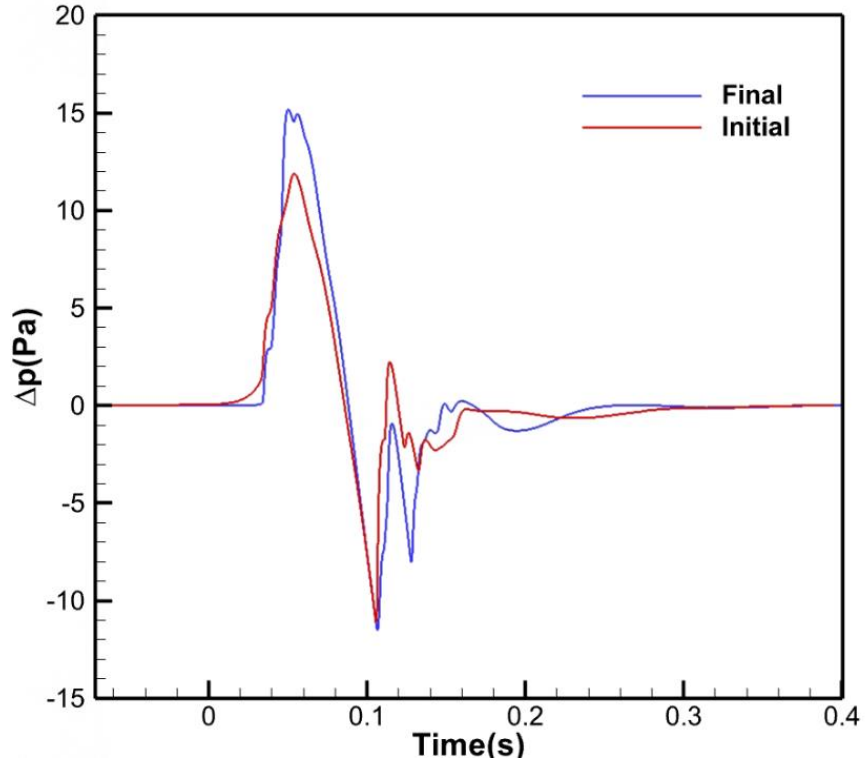


Figure 42 Final adaptive mesh and initial mesh Ground signature comparison of JAXA

Wing, $M=1.6, \alpha=0^\circ, \phi=0^\circ$ at an altitude of 15760 m

The loudness in initial mesh of JWB was 79.98 PLdB while it was 78.50 PLdB in final mesh. In this case, the loudness was decreased because this is a low boom geometry, further improvement in the mesh got more accurate result decreasing the loudness, and we can observe in the Figure 42 that final plot rises up compared to the initial mesh plot.

4.4 JWB: Far field comparison with SBPW2

The Figure 43 compares the initial mesh, final mesh ground signature result with SBPW2 (Atomis CFD) data.

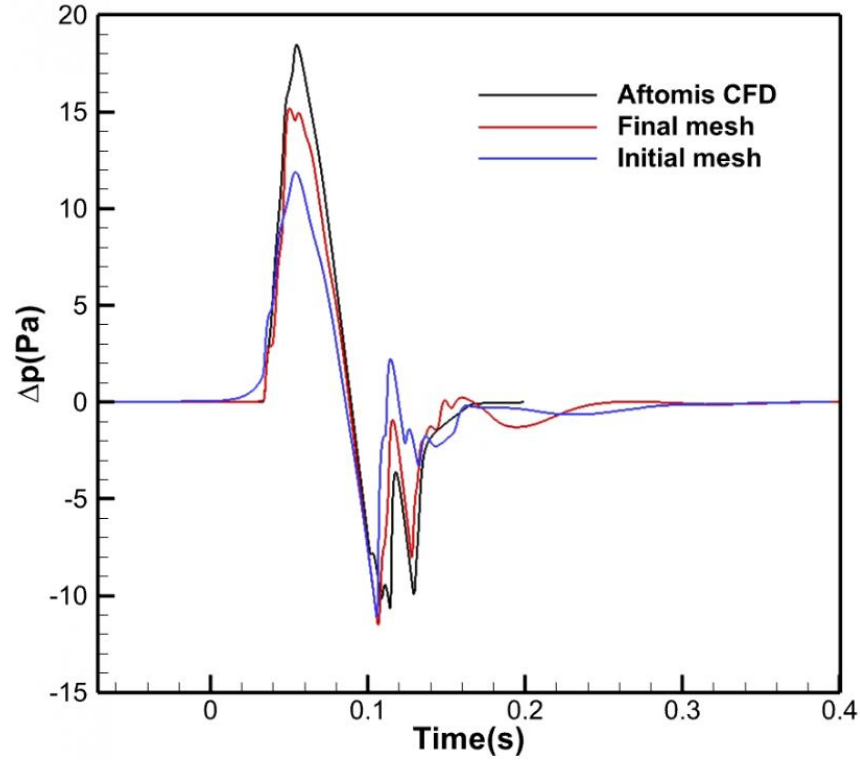


Figure 43 Final adaptive mesh Ground signature comparison of JAXA Wing, My CFD

vs. SBPW2: $M=1.6, \alpha=0^\circ, \phi=0^\circ$ at $H/L= 2.55$

The initial mesh ground signature is smoother and is less accurate while final mesh result rises sharply closely matching the SBPW2(Aftomis CFD) and is more accurate than the initial solution.

Chapter 5 Summary and Outlook

This paper focuses on the problem of excessive sonic boom intensity in the design process of the new generation of supersonic passenger aircraft, and carries out the sonic boom prediction, mainly completed the research work in the following four aspects:

(1) Research on a set of prediction methods for sonic boom suitable for conceptual design and preliminary design of supersonic passenger aircraft.

The importance of supersonic airliner in the future was discussed and why it is a utmost importance to reduce the sonic boom in these supersonic jets to make them viable in the future. Various prediction method and evolution of sonic boom prediction was discussed and the use numerical method or CFD approach was chosen for this study.

(2) The calculation method of near-field sonic boom based on CFD is studied using CFD software.

Cases of first and second sonic boom prediction workshop were selected for this study. Geometry were taken from SBPW websites. The grid generation and flow solution was done using CFD software software. More time was spent on learning the software and grid generation process. Finally the Cartesian mesh with adaptive capability was used and the result of both initial as well as final mesh were compared.

(3) Use of high-precision far-field sonic boom propagation program suitable for detailed design or fine-grained design of supersonic passenger aircraft (bBoom), and studied the influence of calculation parameters and atmospheric effects on the calculation results.

Finally, the near field result obtained was used as input to find the far field solution and loudness of the sonic boom generated by the aircraft flying in the given altitude of each cases. The JWB was better in comparison with DWB in sonic boom and loudness. The DWB model was found to have stronger shocks while the JWB had weaker shocks.

Although the sonic boom from frontal part of the model were easily calculated and was accurate but each signature's aft portion continues to be the most difficult to accurately and inexpensively compute. Wake and plume zones exhibit substantial mesh sensitivity, necessitating much greater resolution (see specifically the JWB case results).

Future work to improve the mesh as well as new techniques to better capture after body propagation and fast and more accurate nearfield solution.

References

- [1] HAN Z, QIAO J, DING Y, et al. Key technologies for next-generation environmentally-friendly supersonic transport aircraft; a review of recent progress[J]. *Acta Aerodynamica Sinica*, 2019: 37 (4): 620-635.
- [2] LEYMAN C. A Review of the Technical Development of Concorde [J]. *Progress in Aerospace Sciences*, 1986: 23(3): 185-238.
- [3] MORGENSTERN J, NORSTRUD N, SOKHEY J, et al. Advanced Concept Studies for Supersonic Commercial Transports Entering Service in the 2018 to 2020 Period Phase I Final Report: NASA CR-217820[R]. Washington, DC: NASA, 2013.
- [4] MORGENSTERN J, BUONANNO M, and YAO J. Advanced Concept Studies for Supersonic Commercial Transports Entering Service in the 2018-2020 Period Phase 2: NASA: NASA CR-218719[R]. Washington, DC: NASA, 2015.
- [5] SUN Y, SMITH H. Review and prospect of supersonic business jet design [J/OL]. *Progress in Aerospace Sciences*, 2017, 90: 12-38. DOI:10.1016/j.paerosci.2016.12.003.
- [6] MAGLIERI D J, BOBBITT P J, PLOTKIN K J. Sonic Boom Six Decades of Research: NASA SP-622[R]. Hampton, VA: NASA: VA: NASA, 2014.
- [7] WHITHAM G. The Flow Pattern of a Supersonic Project [J]. *Communications on Pure and Applied Mathematics*, 1952: 5(3): 301-347.
- [8] HAYES D W. Brief Review of Basic Theory: NASA SP-147[R]. Washington, DC: NASA, 1967.
- [9] CARLSON W H. Simplified Sonic Boom Prediction: NASA TP-1122[R]. Hampton, VA: NASA, 1978.

- [10] SEEBASS R, GEORGE A R. Sonic Boom Minimization [J]. Journal of the Acoustical Society of America, 1972: 49(2C):72.
- [11] CLEVELAND R O, HAMILTON M F, BLACKSTOCK D T. Effect of Stratification and Geometrical Spreading on Sonic Boom Rise Time: NASA N95-14880[R]. Austin, TX: NASA, 1995.
- [12] RALLABHANDI S K. Advanced Sonic Boom Prediction Using the Augmented Burgers Equation [J/OL]. Journal of Aircraft, 2011, 48(4): 1245-1253. DOI:10.2514/1.C031248.
- [13] PARK M A, MORGENSTERN J M. Summary and Statistical Analysis of the First AIAA Sonic Boom Prediction Workshop [J/OL]. 2017. <https://lbpw.larc.nasa.gov/sbpw1/>.
- [14] ANDERSON J D. Computational Fluid Dynamics [M/OL]. McGraw-Hill Education, 1995. <https://books.google.com.sg/books?id=dJceAQAAIAAJ>.
- [15] 朱震浩, 肖天航, 徐雅楠, 邓双厚, 张珍铭, 余雄庆. 基于直角网格伴随自适应的声爆预测 [J]. 北京航空航天大学学报:1-13[2023-06-09]. DOI:10.13700/j.bh.1001-5965.2021.0689.
- [16] XIAO T, QIN N, LUO D, et al. Deformable overset grid for multibody unsteady flow simulation[J]. AIAA Journal, 2016, 54(8):2392–2406.
- [17] HUNTON L W, MENDOXU J P. Some Effects of Wing Planform on Sonic Boom: NASA TN D-7160[R]. NASA, 1973.
- [18] AFTOSMIS M J, NEMEC M. Cart3D Simulations for the First AIAA Sonic Boom Prediction Workshop[C/OL]//52nd Aerospace Sciences Meeting. National Harbor, Maryland: American Institute of Aeronautics and Astronautics, 2014[2023-04-20]. <https://arc.aiaa.org/doi/10.2514/6.2014-0558>. DOI:10.2514/6.2014-0558.

- [19] UENO A, KANAMORI M, MAKINO Y. “Robust Low-Boom Design Based on Near-Field Pressure Signature in Whole Boom Carpet,” [J]. *Journal of Aircraft*, Vol. 54, No. 3, 2017, pp. 925–918. doi:10.2514/1.C033972.
- [20] ORDAZ I, GEISELHART K A, FENBERT J W. “Conceptual Design of Low-Boom Aircraft with Flight Trim Requirement,” [J]. *Journal of Aircraft*, Vol. 52, No. 3, 2015, pp. 932–939. doi:10.2514/1.C033160.
- [21] PARK M A, NEMEC M. Nearfield Summary and Statistical Analysis of the Second AIAA Sonic Boom Prediction Workshop [J/OL]. *Journal of Aircraft*, 2019, 56(3): 851-875. DOI:10.2514/1.C034866.
- [22] CARPENTER F L, CIZMAS P, BOLANDER C R, et al. A Multi-Fidelity Prediction of Aerodynamic and Sonic Boom Characteristics of the JAXA Wing Body [M/OL]//AIAA Aviation 2019 Forum. American Institute of Aeronautics and Astronautics, 2019[2023-06-06]. <https://doi.org/10.2514/6.2019-3237>. DOI:10.2514/6.2019-3237.
- [23] QIAO J, HAN Z, ZHANG L, et al. Far-field sonic boom prediction considering atmospheric turbulence effects: An improved approach [J]. *Chinese Journal of Aeronautics*, 2022, 35(09):208-225.
- [24] Jian-Ling Qiao, Zhonghua Han, Wenping Song and Bi-Feng Song. Development of Sonic Boom Prediction Code for Supersonic Transports Based on Augmented Burgers Equation [J]. IAA 2019-3571. AIAA Aviation 2019 Forum. June 2019.
- [25] Whitham G B. The Behavior of Supersonic Flow Past a Body of Revolution Far from the Axis[J]. *Proceedings of the Royal Society*, 1950, A201(1064): 89-109

- [26] Keller J B. Geometrical Acoustics I, the Theory of Weak Shock Waves[J]. Journal of Applied Physics, 1954, 25(8): 938-947.
- [27] Walkden F. The Shock Pattern of a Wing-Body Combination, Far from the Flight Path[J]. Aeronautical Quarterly, 1958, IX(2):164-194.
- [28] Pestorius M F. Propagation of Plane Acoustic Noise of Finite Amplitude: ARL-TR-73-23 [R]. Arlington, VA: AFOSR, 1973.
- [29] Anderson M O. The Propagation of a Spherical N-Wave in an Absorbing Medium and Its Diffraction by a Circular Aperture: ARL-74-25 [R]. Arlington, VA: AFOSR, 1974.
- [30] Fung K-Y. Shock Wave Formation at a Caustic[J]. SIAM Journal on Applied Mathematics, 1980, 39(2): 355–371.
- [31] Salamone J. Sonic Boom Simulation Using Conventional Audio Equipment: NOISE-CON-2004 [R]. Savannah, GA: Baltimore, Maryland, 2004.
- [32] Friedman M P, Kane E J, Sigalla A. Effects of atmosphere and aircraft motion on the location and intensity of a sonic boom[J]. AIAA Journal, 1963, 1(6): 1327-1335. [47]
- [33] Hayes D W, Haefeli C R, Kulsrud E H. Sonic Boom Propagation in a Stratified Atmosphere, with Computer Program: NASA CR-1299 [R]. Washington, DC: NASA.
- [34] Thomas L C. Extrapolation of Sonic Boom Pressure Signatures by Waveform Parameter Method: NASA TN D-6832 [R]. Washington, DC: NASA, 1972.
- [35] Taylor D A. The TRAPS Sonic Boom Program: NOAA Technical Memorandum ERL ARL-87 [R]. Maryland: Air Resources Laboratories, 1980.
- [36] Plotkin K. PCBoom3 Sonic Boom Prediction Model, Version 1.0e: WR95-22E [R]. Wyle Research, 1998.